The Journal of Immunology

Interorganelle Tethering to Endocytic Organelles Determines Directional Cytokine Transport in CD4$^+$ T Cells

Yan Zhou, Renping Zhao, Eva C. Schwarz, Rahmad Akbar, Mayis Kaba, Varsha Pattu, Volkhard Helms, Heiko Rieger, Paula Nunes-Hasler and Bin Qu

J Immunol published online 26 October 2020
http://www.jimmunol.org/content/early/2020/10/23/jimmunol.2000195

Supplementary Material **http://www.jimmunol.org/content/suppl/2020/10/23/jimmunol.2000195.DCSupplemental**

The Journal of Immunology is published twice each month by
The American Association of Immunologists, Inc.,
1451 Rockville Pike, Suite 650, Rockville, MD 20852

Print ISSN: 0022-1767 Online ISSN: 1550-6606.

Published October 26, 2020, doi:10.4049/jimmunol.2000195

Interorganelle Tethering to Endocytic Organelles Determines Directional Cytokine Transport in CD4$^+$ T Cells

Yan Zhou,*,[1] Renping Zhao,*,[1] Eva C. Schwarz,* Rahmad Akbar,[†] Mayis Kaba,[‡] Varsha Pattu,[§] Volkhard Helms,[†] Heiko Rieger,[¶] Paula Nunes-Hasler,[‡,‖] and Bin Qu*,[#]

Delivery of vesicles to their desired destinations plays a central role in maintaining proper cell functionality. In certain scenarios, depending on loaded cargos, the vesicles have spatially distinct destinations. For example, in T cells, some cytokines (e.g., IL-2) are polarized to the T cell–target cell interface, whereas the other cytokines are delivered multidirectionally (e.g., TNF-α). In this study, we show that in primary human CD4$^+$ T cells, both TNF-α$^+$ and IL-2$^+$ vesicles can tether with endocytic organelles (lysosomes/late endosomes) by forming membrane contact sites. Tethered cytokine-containing vesicle (CytV)–endocytic organelle pairs are released sequentially. Only endocytic organelle-tethered CytVs are preferentially transported to their desired destination. Mathematical models suggest that endocytic organelle tethering could regulate the direction of cytokine transport by selectively attaching different microtubule motor proteins (such as kinesin and dynein) to the corresponding CytVs. These findings establish the previously unknown interorganelle tethering to endocytic organelles as a universal solution for directional cytokine transport in CD4$^+$ T cells. Modulating tethering to endocytic organelles can, therefore, coordinately control directionally distinct cytokine transport. ***The Journal of Immunology*****, 2020, 205: 000–000.**

Cytokines are the key mediators that convey messages between immune cells to orchestrate multifold immune responses against pathogen-infected or tumorigenic cells. Th cells use at least two directionally distinct modes to transport and release cytokines. Certain cytokines are enriched and released at the T cell–target cell contact site, termed immunological synapse (IS), for direct communication with target cells (1–4), for instance, to facilitate B cell Ab isotype switching (5) or to maximize microbicidal activity of macrophages (6). Contrary to the IS-directed release, multidirectional release of cytokines results in systemic immune responses, which is, among others, required to activate cells lacking MHC class II molecules such as CD8$^+$ T cells (7). Directed cytokine transport in Th cells is thus pivotal to guarantee the delivery of functionally distinct cytokines to the right target cells. Examples of polarized secretion toward an APC include IL-2 and, for multidirectional secretion, TNF-α (8).

Tethering between different organelles, which refers to organelles in close proximity to each other featuring physically associated membrane contact sites (MCSs), are identified in mammalian and yeast cells (9). Several well-established MCSs are intensively investigated including endoplasmic reticulum (ER) mitochondria, ER Golgi, ER peroxisome, mitochondria vacuole, mitochondria plasma membrane, and so on (10, 11). In mammalian cells, endocytic organelles, in particular lysosomes/late endosomes, have emerged as a new hub to mediate the formation of MSCs, for instance, with mitochondria, peroxisome, and ER (12–14), the latter two of which are involved in the transport of cholesterol. In immune cells, the juxtaposition of LAMP-1 clusters and lysosomal compartments is observed in NK cells (15), and tethering between lytic granules (LG) and CD3$^+$ endosomes is found in CD8$^+$ T cells (16).

The large protein superfamily of soluble NSF attachment protein receptor (SNARE) proteins mediates vesicle docking, budding, transport, and fusion (17, 18). A few SNARE proteins, for example Sec22b, are reported to mediate ER–plasma membrane tethering (19). Our previous work suggests that the SNARE protein Vti1b mediates LG tethering with CD3 endosomes in CD8$^+$ T cells (16). Vti1b also mediates homotypic late endosome fusion or heterotypic late endosome–lysosome fusion together with its interacting SNARE partners syntaxin 7, syntaxin 8, VAMP7, or VAMP8 (20). In addition, compelling evidence proves that the clathrin adaptor EpsinR (also known as CLINT1), the interaction partner of

*Department of Biophysics, Center for Integrative Physiology and Molecular Medicine, School of Medicine, Saarland University, 66421 Homburg, Germany; [†]Center for Bioinformatics, Saarland University, 66123 Saarbrücken, Germany; [‡]Department of Cell Physiology and Metabolism, University Medical Center, University of Geneva, 1211 Geneva, Switzerland; [§]Department of Physiology, Center for Integrative Physiology and Molecular Medicine, School of Medicine, Saarland University, 66421 Homburg, Germany; [¶]Department of Theoretical Physics, Saarland University, 66123 Saarbrücken, Germany; [‖]Department of Pathology and Immunology, University Medical Center, University of Geneva, 1211 Geneva, Switzerland; and [#]Leibniz Institute for New Materials, 66123 Saarbrücken, Germany

[1]Y.Z. and R.Z. contributed equally.

ORCIDs: 0000-0002-6503-4864 (E.C.S.); 0000-0002-6692-0876 (R.A.); 0000-0002-2180-9154 (V.H.); 0000-0002-4598-685X (P.N.-H.); 0000-0002-9382-3203 (B.Q.).

Received for publication February 20, 2020. Accepted for publication September 20, 2020.

This work was funded by the Deutsche Forschungsgemeinschaft (Projects SFB1027 A2 [to B.Q.], SFB1027 A3 [to H.R.], and SFB1027 C3 [to V.H.]) and by the Leibniz Association (INM Fellow to B.Q.). P.N.-H. is supported by the Novartis Foundation (Grant 17B078), the Prof. Dr. Max Cloëtta Foundation 2019 Medical Researcher Award, and the Swiss National Science Foundation (Grant 310030_189094).

Address correspondence and reprint requests to Dr. Bin Qu, Department of Biophysics, Center for Integrative Physiology and Molecular Medicine, School of Medicine, Building 48, Saarland University, 66421 Homburg, Germany. E-mail address: bin.qu@uks.eu

The online version of this article contains supplemental material.

Abbreviations used in this article: CLEM, correlative light and electron microscopy; co-IP, coimmunoprecipitation; CytV, cytokine-containing vesicle; dist, distal area; EM, electron microscopy; ER, endoplasmic reticulum; F, forward; IS, immunological synapse; LCSM, laser confocal scanning microscopy; LG, lytic granule; MCS, membrane contact site; MTOC, microtubule organizing center; N.A., numerical aperture; PDB, Protein Data Bank; R, reverse; SIM, structured illumination microscopy; siRNA, small interfering RNA; SNARE, soluble NSF attachment protein receptor; TIRF, total internal reflection fluorescence; WT, wild-type.

Vti1b, is essential for sorting Vti1b to the corresponding vesicles (21–23).

In this work, using multiple forms of advanced microscopy, we show that in primary human CD4$^+$ T cells, both TNF-α$^+$ and IL-2$^+$ vesicles can tether with endocytic organelles. Only endocytic organelle-tethered cytokine-containing vesicles (CytVs) are preferentially transported to their desired destination, suggesting this interorganelle tethering as a universal solution for directionally distinctive cytokine transport. Mathematical models suggest that selectively attaching different microtubule motor proteins (such as kinesin and dynein) mediated by endocytic organelle tethering could be a mechanism to direct the transport of the corresponding CytVs. Together, our work reveals that a previously unknown interorganelle tethering to lysosomes plays a central role in regulating directional cytokine transport in CD4$^+$ T cells.

Materials and Methods

Abs and reagents

All chemicals not specifically mentioned were from Sigma-Aldrich (highest grade). For immunostaining and/or Western blot, the following Abs were used: Alexa Fluor 647–labeled anti-human TNF-α mAb (MAb11; BioLegend), Brilliant Violet 421– or Alexa Fluor 488–labeled anti-human LAMP1 mAb (H4A3; BioLegend), Alexa Fluor 647–labeled anti-human IL-2 mAb (MQ1-17H12; BioLegend), rabbit polyclonal anti-Vti1b Ab (Synaptic Systems), anticytoplasmic dynein intermediate chain mAb (74.1; BioLegend), anti-kinesin H chain mAb (SUK-4; BioLegend), Alexa Fluor 488 phalloidin (Thermo Fisher Scientific), Alexa Fluor 568 phalloidin (Thermo Fisher Scientific), Alexa Fluor 568 goat anti-rabbit secondary Ab (Thermo Fisher Scientific), and anti–γ-tubulin Ab (Sigma-Aldrich). For coating coverslips, the Abs against human CD3 (BB11; Diaclone) and CD28 (BD Bioscience) were used. Modified small interfering RNA (siRNA) against Vti1b (Vti1B_8_4479; QIAGEN) and control siRNA were purchased from QIAGEN as described in (16). For coimmunoprecipitation (co-IP), GFP-Trap_A (Chromotek) was used for one-step immunoprecipitation, and polyclonal rabbit anti-CLINT1 (EpsinR) (Abcam) was used for Western blot.

CD4$^+$ T cell preparation, cell culture, and nucleofection of T cells

PBMC were obtained from healthy donors as described in Ref. 24. Untouched CD4$^+$ T cells were isolated from PBMC using a CD4 negative isolation kit (Dynabeads Untouched Human CD4 T Cells; Thermo Fisher Scientific) and stimulated with Dynabeads Human T-Activator CD3/CD28 (Thermo Fisher Scientific). For transfection, 48 h after, stimulation beads were removed, and 5×10^6 CD4$^+$ T cells were nucleofected with plasmid (1 μg) or siRNA (10 μl of 20 μM) using the P3 Primary Cell 4D-Nucleofector Kit (Lonza). Medium was changed 6–12 h after nucleofection, and the transfected CD4$^+$ T cells were maintained in AIM V medium (Thermo Fisher Scientific) with 10% FCS and 30 U/ml of recombinant human IL-2 (Thermo Fisher Scientific). Cells were used 24–48 h (plasmids) or 36 h (siRNA) after nucleofection for experiments if not mentioned otherwise. Raji cells were cultured in RPMI 1640 medium (Thermo Fisher Scientific) with 10% FCS and 1% penicillin/streptomycin. HEK293T cells were cultured in DMEM medium (Thermo Fisher Scientific) with 10% FCS and 1% penicillin/streptomycin.

DNA constructs

TNF-α, IL-2, and Vti1b were cloned from human cDNA, referring to the cDNA sequence NM_000594.3, NM_000586.3, and NM_006370.2, respectively. pMax-TFP- and pMax-mCherry-TNF-α were produced by PCR and ligated into BamHI and XhoI sites of modified pMax vector with TFP or mCherry at the N terminus. pMax-IL-2-mCherry was produced with PCR and cloned into EcoRI and BamHI sites of pMax construct with mCherry at the C terminus. pMax-TFP/mCherry-Vti1b FL and TFP-Vti1b 1–207 were produced by PCR and ligated into BamHI and XhoI sites of modified pMax vector with TFP or mCherry at the N terminus. pMax-GFP/mCherry-Vti1b E12A and F73S were generated by PCR-mediated mutagenesis. mCherry-Rab5a, mCherry-Rab7a, and mCherry-Rab11a were a kind gift from Jens Rettig (Saarland University). LAMP1-EGFP and CD63-EGFP were a kind gift from Lei Lu (Nanyang Technological University). The authenticity of the DNA sequences was confirmed by sequencing.

Epifluorescence deconvolution microscopy and immunofluorescence

CD4$^+$ T cells were settled on anti-CD3/anti-CD28 Ab-coated coverslips or with target cells at 37°C for the indicated period of time and then fixed with prechilled 4% paraformaldehyde. Samples were imaged with a Zeiss Cell Observer HS system. For fixed cells, the following single bandpass filter sets were used: GFP (38HE; Zeiss), ET-Texas Red (Chroma Technology), DAPI HE (Zeiss), Texas Red HE (Zeiss), and Cy 5 HE (Zeiss) filter sets. Images were acquired with a 63× αPlan-Fluor Objective (numerical aperture [N.A.] 1.4) and an AxioCam MRm Rev 3 with binning 1 × 1 and a z-step size of 0.2 μm. For time-lapse imaging, the filter set was a Zeiss 62 HE triple band with single excitation filters inside the fast-wavelength switching xenon burner DG-4 (Sutter Instrument). The acquired images were preceded for deconvolution with the Huygens Essential program by using a theoretical point spread function. To quantify vesicle fusion, the time points of release were determined by the fluorescence peaks right before the drop of fluorescence.

Structured illumination microscopy

Images were taken by a structured illumination microscopy (SIM) setup (ELYRA PS.1; Zeiss) with a 63× Plan-Apochromat (N.A. 1.4) with an excitation light of 488, 568, and 635 nm wavelengths, and ZEN 2012 software was used for acquisition and processing of the images for higher resolution as reported by Gustafsson et al. (25). Z-stacks of 200-nm step size were used to scan the entire cell.

Laser scanning confocal microscopy imaging

Primary human CD4$^+$ T cells were stimulated with anti-CD3/anti-CD28 Ab-coated beads. On day 2, the beads were removed, and the T cells were transfected with LAMP1-EGFP and mCherry-TNF-α in tandem. Sixteen hours posttransfection, the T cells were settled on an anti-CD3/anti-CD28 Ab-coated coverslip. Images were acquired at room temperature with an interval of 1 s by confocal microscopy LSM 710 with a ×63 objective (N.A. 1.4) and a Nikon E600 camera using ZEN software.

Tethering analysis

The fraction of tethered vesicles was analyzed as described in Ref. 16. Briefly, deconvoluted images were analyzed with ImageJ software to ensure the same setting for the fluorescence intensity of cytokine carrier and lysosomes. Tethering was analyzed and counted from one stack to another. No matter how many lysosomes the cytokine vesicle was tethered with, it was counted only once as a tethered vesicle. The cloud-like structures at the centrosomal area are excluded. The fraction of tethered vesicles was calculated as (number of tethered vesicle/number of total vesicle) × 100%. In addition, the results of automated analysis were double checked manually.

Correlative light and electron microscopy

Correlation light and electron microscopy (CLEM) was performed as previously described (26). Briefly, day 3 stimulated human primary CD4$^+$ T cells expressing mCherry-IL-2 and LAMP1-EGFP were seeded on 35-mm optical polymer bottom μ-Dish Grid 500 culture dishes (Ibidi) and fixed in 4% paraformaldehyde/PBS. High-resolution and low-resolution fluorescence and brightfield images were then acquired using a deconvolution microscope. Once the imaging was completed, the dish was washed in PBS and fixed in a buffer with 2.5% glutaraldehyde/2% paraformaldehyde, 2 mM $CaCl_2$, and 0.15 M cacodylate (pH 7.4) for 3 h on ice and washed five times in cold cacodylate. The dish was then stained and embedded for focused ion beam scanning EM imaging as previously described (27). Samples were mounted on an aluminum pin using Pelco C100 cyanoacrylate glue and Pelco conductive silver paint (Ted 583; Ted Pella) and sputter coated with gold for 30 s using a Q150T ES coater (Quorum Technologies). Focused ion beam scanning EM imaging was performed on a Helios NanoLab G3 microscope (FEI). Images were acquired at the highest resolution setting, resulting in 3.18 × 3.18 nm pixels, using the electron beam at 2 kV/0.4 nA, and milling sections with the ion beam at 30 kV/2.5 nA every 10 nm using the AutoSlice and View software (FEI).

Total internal reflection fluorescence microscopy imaging

Total internal reflection fluorescence (TIRF) microscopy images were acquired using a Leica DMI6000 B TIRF MC microscope (Leica Microsystems) equipped with a high-speed EM charge-coupled device camera (C9100-02; Hamamatsu Photonics), an HCX Plan-Apochromat ×100 objective lens (N.A. 1.46; Leica Microsystems), and Leica AF6000 software. During acquisition, cells were kept in Ringer solution without

calcium and followed by perfusion with Ringer solution containing 0.5 mM Ca^{2+} or 10 mM Ca^{2+} at 37°C or room temperature as indicated in the figure legends. Two-color acquisition was achieved by fast switching excitation lasers so that images from green and red channels were aligned perfectly. Live-cell imaging was recorded for 10 min by TIRF microscopy at excitation wavelengths of 488 and 561 nm, respectively. The acquisition speed was around 7 Hz, and the exposure time was around 70 ms for each channel. Images were analyzed with ImageJ software.

Western blot and co-IP

Proteins were separated by SDS-PAGE and transferred to polyvinylidene difluoride membranes. After blocking with 5% nonfat milk, membranes were incubated with primary Abs (anti-Vti1b and anti–γ-tubulin), followed by corresponding HRP-conjugated secondary Abs. Target proteins were detected using an ECL kit (ECL Detection Kit; Amersham Biosciences). HEK293T cells overexpressing GFP-tagged Vti1b (wild-type [WT] or mutants) were lysed with lysis buffer and the lysate was incubated with GFP-Trap-A (Chromotek) for 4 h at 4°C. Afterward, the GFP-Trap was washed, and Western blot was performed with anti-CLINT1 Ab.

Quantitative real-time PCR

$CD4^+$ T cells were harvested at the indicated time points, and RNA isolation with TRIzol Reagent (Thermo Fisher Scientific) was performed according to the manufacturer's instructions. cDNA was synthesized from RNA via reverse (R) transcription using SuperScript II R Transcriptase (Thermo Fisher Scientific). Afterward, real-time PCR was carried out in a CFX96 Real-Time System C1000 Thermal Cycler (Software Biorad CFX Manager, Version 3.0) using QuantiTect SYBR Green Kit (QIAGEN). Sequences of primers used for TNF-α forward (F): 5′-CCTCTCTCTAATCAGCCCTCTG-3′, TNF-α R: 5′-GAGGAC CTGGGAGTAGATGAG-3′; IL-2 F: 5′-TCCTGTCTTGCATTGCACTAAG-3′, IL-2 R: 5′-CAT CCTGGTGAGTTTGGGATTC-3′; and Vti1b F: 5′-ATATATGCTGTAGAGAATG AGC-3′, Vti1b R: 5′-TGGAAAGCAGCAGCTTGTTG-3′.

Data analysis

Data were analyzed using ImageJ v1.50g, AxioVision (Zeiss), Microsoft Excel (Microsoft), and Huygens deconvolution (Scientific Volume Imaging). For CLEM, drift correction, reslicing, and alignment were performed using Amira, ImageJ, and CorelDraw software, respectively. The statistical differences were analyzed with GraphPad Prism 6.0 using Student *t* test if not otherwise mentioned. All values are given as mean ± SEM if not otherwise mentioned: $*p < 0.05$, $**p < 0.01$, and $***p < 0.001$.

Prediction of essential residues for the interaction between Vti1b and its cognate SNAREs

At first, we evaluated the suitability of several computational tools to predict the energetic effects of mutations on the stability of SNARE protein. For this, we retrieved the coordinate file of an atomistic x-ray structure of the complex of the Vti1b protein with EpsinR (23) (Protein Data Bank [PDB] identifier 2V8S) from the PDB (28). The energetic effects of hypothetically engineered alanine point mutations were predicted using the three programs: MAESTRO (29), ROSETTA (30), and BeAtMuSiC (31). MAESTRO approximates a change in protein stability (ΔΔG) due to a point mutation by a machine learning approach. ROSETTA and BeAtMuSiC use statistically derived potentials to estimate the effect of the protein mutation on the binding affinity of the complex. Results from the predictions were compared with the experimental observations of Miller et al. (23) who reported that mutating positions S8W, E12A, E65W, and F73S of Vti1b and of F52D, M53D, Y54D, and R96S on EpsinR strongly disfavored formation of their complex. As shown in Supplemental Table I, BeAtMuSiC, when applied to the 2V8S structure, assigned positive (i.e., destabilizing) ΔΔG values to seven out of eight of these residues with an average ΔΔG value of 1.95 kcal/mol. MAESTRO assigned positive ΔΔG values to four of these residues (average 1.26 kcal/mol), and ROSETTA to none of these (average −0.02 kcal/mol). Hence, we selected the BeAtMuSiC tool to predict the unknown effects of point mutations in an endosomal SNARE core complex. For this purpose, we retrieved the coordinate file of an atomistic x-ray structure of the endosomal SNARE core complex containing Vti1b (PDB identifier 1GL2) (32) from the PDB. The complex comprises four chains: A (Endobrevin/VAMP8), B (Syntaxin7), C (Vti1b), and D (Syntaxin8). The following pairs involving Vti1b were analyzed: Endobrevin–Vti1b, Syntaxin7–Vti1b, and Syntaxin8–Vti1b. The predicted changes in binding affinity upon hypothetical alanine point mutations introduced to residues at the binding interface were then predicted for these pairs using BeAtMuSiC (Supplemental Table II).

Ethical considerations

Research carried out for this study with human material (leukocyte reduction system chambers from human blood donors) was authorized by the local ethics committee (declaration from 16.4.2015 [84/15; Prof. Dr. Rettig-Stürmer]).

Results

Transport of TNF-α and IL-2 is directionally distinct

To investigate the transportation of cytokines, we focused on TNF-α and IL-2 as representative examples. We used primary human $CD4^+$ T cells stimulated with anti-CD3/anti-CD28 Ab-coated beads. We found that in these T cells, both TNF-α and IL-2 are upregulated upon IS formation of T cells with anti-CD3/anti-CD28 Ab-coated coverslips. TNF-α mRNA level was already enhanced 30 min after IS formation (Supplemental Fig. 1A), whereas the first peak of IL-2 mRNA appeared at 60 min after IS formation (Supplemental Fig. 1B). Quantification of immunostaining shows that the expression of endogenous IL-2 is initiated later than TNF-α and reached a comparable level of TNF-α 2 h after IS formation (Supplemental Fig. 1C).

Next, we verified the localization of endogenous TNF-α and IL-2 in primary human $CD4^+$ T cells at various time points upon IS formation. We settled $CD4^+$ T cells on glass coverslips coated with anti-CD3/anti-CD28 Abs to obtain a spatially well-defined IS between the T cell and the coverslip. Deconvolution microscopy results show that TNF-α first appeared in a condensed structure in vicinity to the IS, and then TNF-α–containing vesicles (hereafter referred to as TNF-α^+ vesicles) were transported multidirectionally (Fig. 1A, upper panel). The condensed structure is colocalized with Golgi marker GM130 (Supplemental Fig. 1D). In comparison with TNF-α, endogenous IL-2 first appeared 60 min after activation and is mainly accumulated at the IS (Fig. 1A, lower panel). Further analysis of the distribution of endogenous TNF-α and IL-2 in the same T cells (Fig. 1B) showed that at 60 min after IS formation, ∼50% of the TNF-α^+ vesicles were at the IS. With time, at 90 min, fewer TNF-α^+ vesicles (∼38%) stayed at the IS; in other words, more TNF-α^+ vesicles were transported away from the IS (i.e., multidirectionally). In contrast, IL-2^+ vesicles were enriched at the IS already at early time points (60 min, 58%), and their number further increased with time (90 min, ∼64%/120 min, ∼61%). In conclusion, simultaneous recordings from the same cell revealed that, at later time points, IL-2 is enriched at the IS, whereas TNF-α is more multidirectionally distributed, which was especially prominent at 90 min. We noticed that at 120 min, the fraction of TNF-α at the IS was slightly enhanced compared with 90 min. This might be due to newly generated TNF-α^+ vesicles or the release of TNF-α^+ vesicles away from the IS. Thus, we confirm that transportation of TNF-α and IL-2 is directionally different, namely TNF-α multidirectionally and IL-2 to the IS.

CytVs are tethered with lysosomes/late endosomes

To reveal how this directionally distinct transport of CytVs is regulated, we examined their subcellular localization. Various organelle markers, such as early (Rab5), late (Rab7), recycling endosomes (Rab11), or lysosomes (LAMP1), were cotransfected with fluorescently tagged TNF-α. We found that TNF-α^+ vesicles were positioned in close vicinity to particular endosomal compartments, especially late endosomes (Rab7a$^+$) and lysosomes (LAMP1$^+$) (Fig. 1C, 1D). This consistent juxtaposition of the two vesicles suggests that they may be physically tethered.

To distinguish whether Rab7a and LAMP1 compartments colocalize or tether independently with TNF-α^+ vesicles, we cotransfected mCherry-Rab7a and LAMP1-EGFP in bead-activated $CD4^+$ T cells. We observed that a large proportion of Rab7a colocalized with

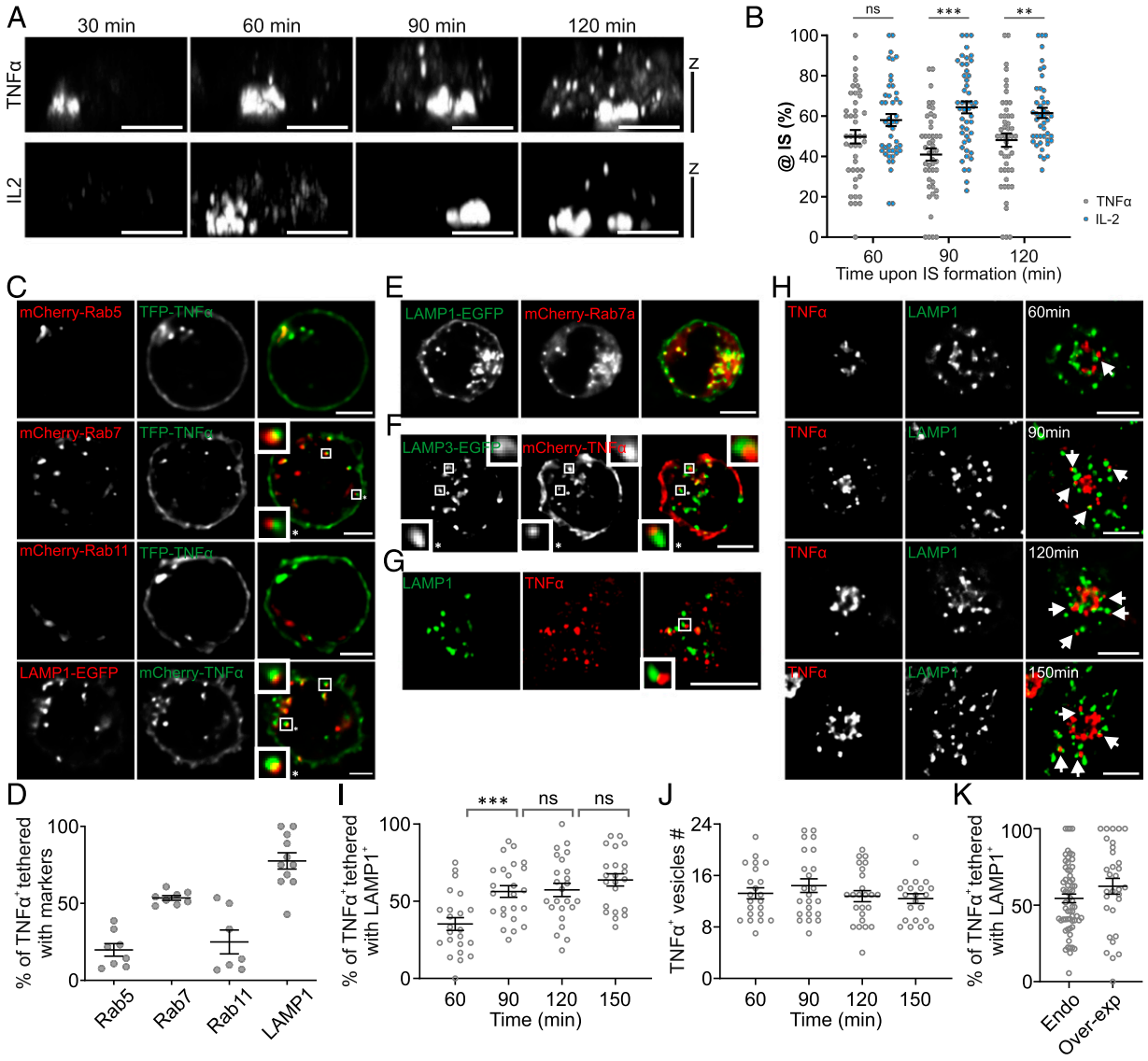

FIGURE 1. TNF-α$^+$ vesicles are juxtaposed to endocytic organelles. (**A** and **B**) TNF-α$^+$ vesicles and IL-2$^+$ vesicles are distinctively transported after IS formation. CD4$^+$ T cells were settled on CD3/CD28 Ab-coated coverslips. Endogenous TNF-α or IL-2 was stained with corresponding mAb conjugated with Alexa Fluor 488 or Alexa Fluor 647. Maximum intensity projections (MIP) of the exemplary cells from three independent experiments are shown in (A). Quantification of distribution of TNF-α and IL-2 in the same T cells is shown in (B). The segment encompassing one fourth of the cell's diameter close to the coverslip was defined as IS area (@IS). The fraction of IL-2 or TNF-α (percentage of total number) was analyzed from three independent experiments. Mann–Whitney *U* test was used. (**C** and **D**) Subcellular localization of TNF-α in primary human CD4$^+$ T cells. Fluorescently tagged TNF-α and indicated markers for each particular intracellular compartment were transiently overexpressed in stimulated CD4$^+$ T cells. Quantification of the tethering rate of TNF-α$^+$ vesicles with endosomal markers is shown in (D) (from two independent experiments). (**E**) Colocalization of Rab7a and LAMP1. Anti-CD3/anti-CD28 Ab-coated beads–stimulated primary human CD4$^+$ T cells were transiently overexpressed with LAMP1-EGFP and mCherry-Rab7a. One representative cell out of two independent experiments is shown. (**F**) TNF-α$^+$ vesicles are tethered with LAMP3. Stimulated primary human CD4$^+$ T cells transiently overexpressing mCherry-TNF-α and LAMP3-EGFP (n = 3 independent experiments). The samples in (A)–(F) were scanned by deconvolution microscopy with a ×63 objective. (**G**) Endogenous TNF-α and LAMP1 were stained with Alexa Fluor 647–labeled anti-human TNF-α mAb and Alexa Fluor 488–labeled anti-human LAMP1 mAb. The samples were scanned by superresolution SIM with a ×63 objective. One representative cell out of three independent experiments is shown. (**H**–**J**) TNF-α–lysosome tethering is increased with time upon stimulation. Bead-stimulated CD4$^+$ T cells were settled on anti-CD3/anti-CD28 Ab-coated coverslips and fixed at indicated time points. Exemplary cells are shown in (H). The fractions of TNF-α$^+$ vesicles tethered with LAMP1$^+$ vesicles and the numbers of TNF-α$^+$ vesicles are shown in (I) and (J), respectively. Twenty-four cells from three independent experiments were analyzed. (**K**). The tethering rate was not affected by overexpression of TNF-α. Results of endogenous and overexpressed TNF-α are from six and five independent experiments, respectively. Scale bars, 5 μm, except in (C) (3 μm). $^{**}p < 0.01$, $^{***}p < 0.001$.

LAMP1 (Fig. 1E, Pearson correlation coefficient = 0.78 ± 0.05, n = 10). To further explore to which organelle type TNF-α$^+$ vesicles are juxtaposed, we used LAMP3 (CD63), another marker for lysosomes. We found that the LAMP3$^+$ compartment was also juxtaposed to TNF-α$^+$ vesicles (Fig. 1F). To investigate whether endogenous TNF-α$^+$ vesicles are also juxtaposed to lysosomes, we used superresolution SIM. We observed the vesicles containing endogenous TNF-α to be in close vicinity of lysosomes marked by endogenous LAMP1 (Fig. 1G). Thus, we conclude that TNF-α$^+$ vesicles are juxtaposed to late endosomes/lysosomes. Hereafter, we used LAMP1 as the marker for late endosomes/lysosomes.

Next, we analyzed whether this juxtaposition could be changed over time upon IS formation. The immunostaining results show that the percentage of endogenous TNF-α juxtaposed to lysosomes was significantly increased from <40% at 60 min to around 60% at 90 min after IS formation and stayed relatively stable afterward (Fig. 1H, 1I).

The total numbers of TNF-α$^+$ vesicles remained unchanged during this period of time (Fig. 1J). In addition, we found no difference in the fraction of LAMP1-tethered TNF-α between endogenous and overexpression cases (Fig. 1K), indicating that overexpression of TNF-α does not change the tethering rate. These results suggest that tethering between lysosomes and TNF-α$^+$ vesicles may be promoted by IS formation.

Considering that the transport patterns of TNF-α (multidirectional) and IL-2 (IS polarized) are different, we hypothesized that, in contrast to TNF-α$^+$ vesicles, IL-2$^+$ vesicles will not tether with endocytic organelles. However, we found that the vesicles containing endogenous IL-2 were also juxtaposed to LAMP1$^+$ organelles at all time points examined upon the formation of IS with no significant difference (Fig. 2A, 2B). Noticeably, the overall number of IL-2$^+$ vesicles was decreased at 150 min compared with earlier time points (Fig. 2C), likely because of their release. To establish whether the two organelles were truly close enough to be physically tethered to one another, we performed CLEM. We found that fluorescently detected mCherry-IL-2/LAMP1-EGFP vesicle pairs could be resolved as two tethered vesicles with a physical attachment in the higher-magnification EM images (Fig. 2D, 2E). The distance between these tethered vesicles is 26.6 ± 3.0 nm (n = 10), which is within the range of MCSs to define interorganelle tethering (9, 10). In addition, small regions of electron-dense accumulations, which are characteristic of MCSs (33) and are thought to represent protein tethering complexes, can be discerned at the site of contact between lysosomes and CytVs (Fig. 2E, arrowheads). Thus, together, these data demonstrate that CytVs can physically tether with LAMP1$^+$ organelles.

Tethered CytV–lysosome pairs are transported in tandem and released sequentially

To exclude the possibility that tethering is an artifact introduced by fixation, we examined tethering in live CD4$^+$ T cells by live-cell imaging. To be able to track the tethered TNF-α–LAMP1 pairs for a considerably long period of time, we used TIRF microscopy. With TIRF, only a thin layer of around 200 nm above the glass coverslip is illuminated. We observed that tethered TNF-α–LAMP1 pairs were transported in tandem (Fig. 3A, Supplemental Video 1). Remarkably, on rare occasions, we observed that after a short contact with another TNF-α–lysosome pair, the transport of a tethered TNF-α–lysosome pair could be switched to the opposite direction (Fig. 3B, Supplemental Video 2). Next, we examined the cotransport of IL-2–LAMP1 pairs using laser confocal scanning microscopy (LCSM). Live-cell imaging shows that tethered IL-2 and LAMP1 vesicles were also transported in a tandem manner (Fig. 3C, Supplemental Video 3). Very occasionally, separation of CytV–LAMP1 pairs was detected (Fig. 3D, Supplemental Video 4). Thus, we demonstrate that CytV–lysosome tethering is present in live cells and is not an artifact of fixation.

We next examined if and how CytV–lysosome pairs are released. We examined TNF-α–lysosome pairs with high frequency time-lapse imaging (~7 Hz) using TIRF. We found that after docking at the plasma membrane, TNF-α fluorescence vanished first followed by the fusion of the tethered lysosome (Fig. 3E, 3F, Supplemental Videos 5 and 6). Notably, after the release of TNF-α was initiated, as indicated by a sharp drop of the mCherry (TNF-α) fluorescence, the fluorescence intensity of LAMP1$^+$ vesicles at the TIRF plane was first intensified (highlighted by the light green boxes) and then gradually declined with time (Fig. 3E, 3F). The increase in fluorescence of the second vesicle suggests that the vesicle moves closer to the TIRF plane because the intensity of illumination by the evanescent field would increase exponentially with the distance (34). Thus, these results indicate that tethered TNF-α$^+$ and LAMP1$^+$ vesicles are released sequentially. Notably, as shown in these two examples, TNF-α and LAMP1 fluorescence often appeared to be highly colocalized, which could be the result of a quasiperpendicular spatial orientation of the tethered TNF-α–LAMP1 pairs with respect to the plasma membrane. More precisely speaking, as sketched in Fig. 3E, 3F, if LAMP1$^+$ vesicles are positioned on top of the TNF-α$^+$ vesicles, when the latter is docked at the plasma membrane, the fluorescence from TNF-α$^+$ and LAMP1$^+$ vesicles would be largely overlapped when observed at the TIRF plane.

To test this hypothesis, we needed to be able to distinguish simultaneous release from sequential release. The former would be

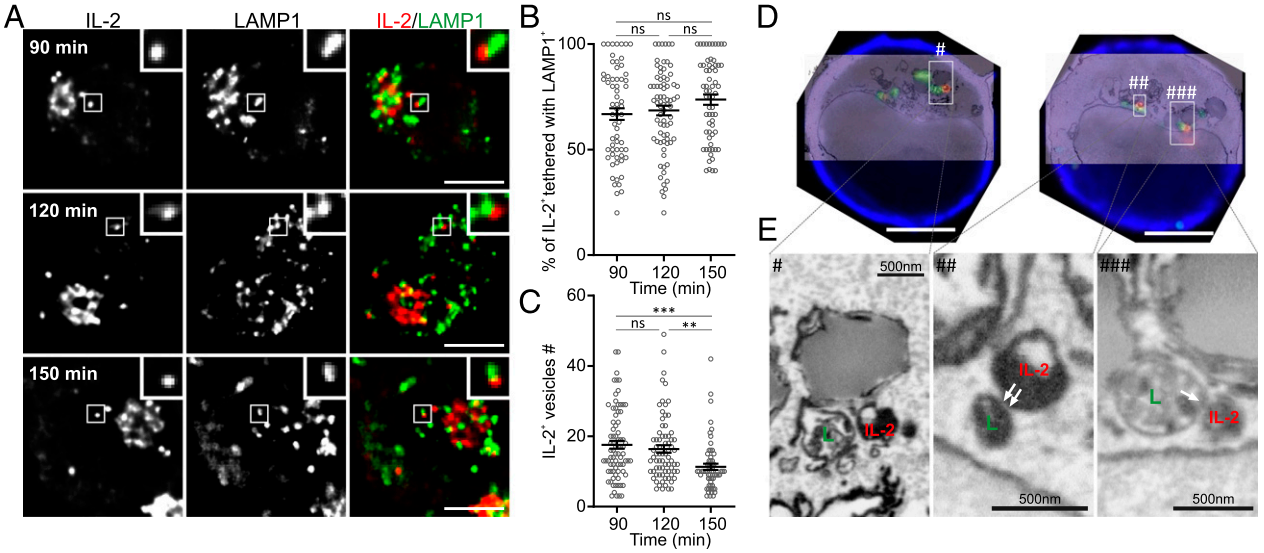

FIGURE 2. IL-2$^+$ vesicles are tethered to LAMP1$^+$ vesicles. (**A**–**C**) IL-2$^+$ vesicles are juxtaposed to LAMP1$^+$ vesicles. Endogenous IL-2 and LAMP1 were stained with Alexa Fluor 647–labeled anti-human IL-2 mAb and Alexa Fluor 488–labeled anti-human LAMP1 mAb. The tethering rate of IL-2$^+$ vesicles with LAMP1$^+$ organelles and the total number of IL-2$^+$ vesicles are shown in (B) and (C), respectively. The results for 90, 120, and 150 min were from five donors (79 cells), five donors (75 cells), or four donors (64 cells), respectively. (**D** and **E**) IL-2$^+$ vesicles physically tether with LAMP1$^+$ vesicles. CD4$^+$ T cells were cotransfected with mCherry-IL-2 and LAMP1-EGFP. CLEM was performed to examine the localization of IL-2$^+$ vesicles (red) and LAMP1$^+$ lysosomes (green). Arrowheads highlight the small regions of electron-dense accumulations. Three examples of tethered IL-2–lysosome pairs are shown. Two exemplary cells from two independent experiments are shown. Scale bars, 5 μm (A and D) or 500 nm (E). $^{**}p < 0.01$, $^{***}p < 0.001$.

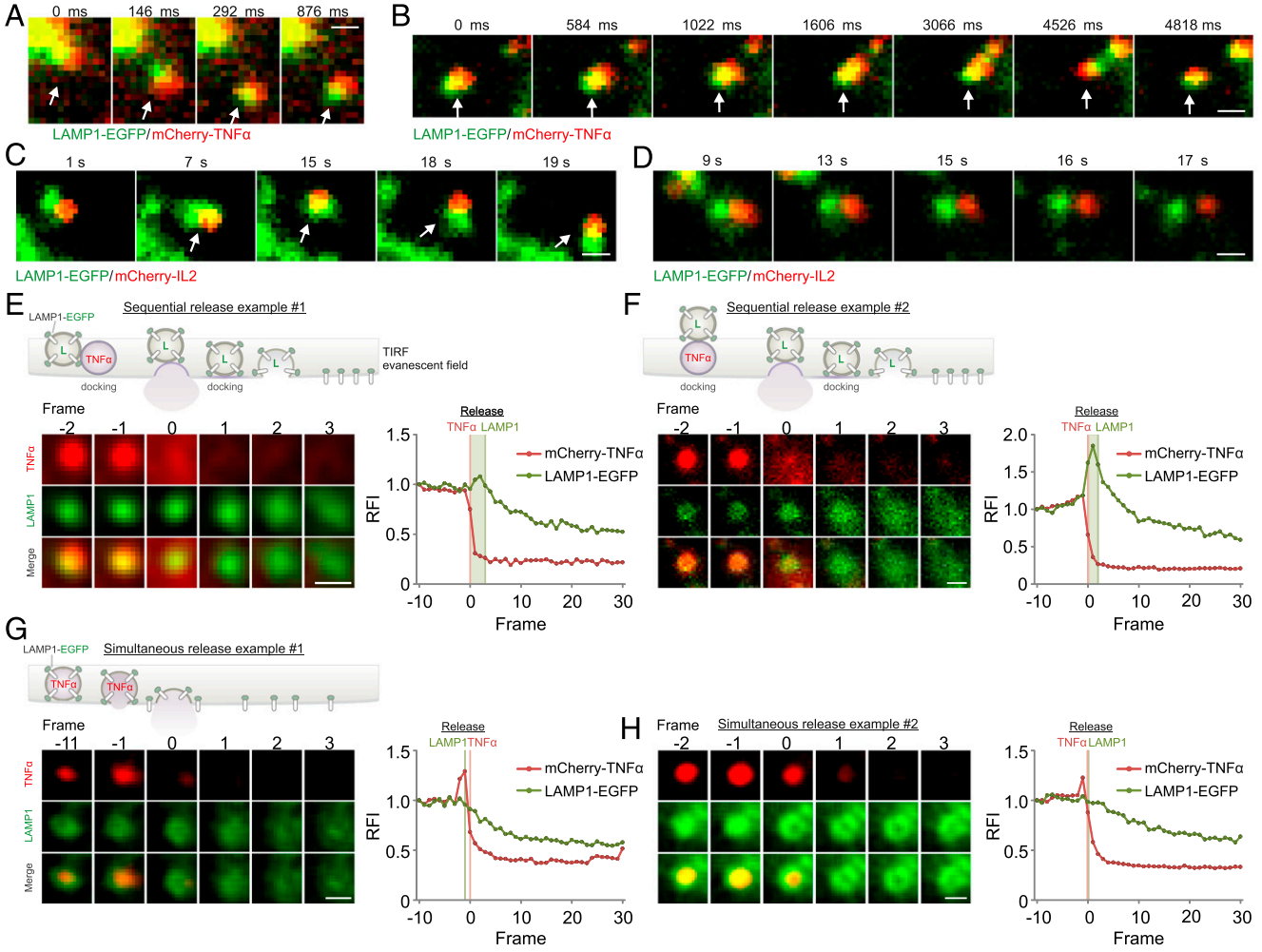

FIGURE 3. Cotransportation and sequential release of tethered CytV–LAMP1$^+$ vesicles. LAMP1-EGFP and mCherry-TNF-α or mCherry-IL-2 as indicated were cotransfected in primary human CD4$^+$ T cells. (**A** and **B**) Tethered TNF-α–LAMP1$^+$ vesicles were transported in tandem. (**C**) Cotransportation of tethered IL-2–LAMP1$^+$ vesicles. (**D**) Separation of tethered IL-2–LAMP1$^+$ vesicles. (**E** and **F**) Sequential secretion of tethered TNF-α–LAMP1$^+$ vesicles. The frame, at which TNF-α$^+$ or LAMP1$^+$ vesicles was released, is marked by red or green lines. Increase in LAMP1 fluorescence at the TIRF plane after TNF-α fusion is highlighted by the green boxes. (**G** and **H**) Two examples of simultaneous release of colocalized TNF-α and LAMP1. Transportation and release of vesicles were visualized at room temperature using either TIRF with a ×100 objective with an interval of 146 ms (A, B, and E–H) or with laser scanning confocal microscopy with an interval of 1 s (C and D). The CD4$^+$ T cells were settled either on anti-CD3/anti-CD28 Ab-coated coverslips (A, B, and E–H) or on poly-L-ornithin–coated coverslips (C and D). All results are from three independent experiments. Scale bar, 1 μm.

the consequence of the release of truly colocalized TNF-α$^+$ and LAMP1$^+$ vesicles. In transfected CD4$^+$ T cells, colocalization of TNF-α–LAMP1 was indeed observed on some occasions. Especially when the overexpression level of LAMP1 was high, TNF-α was observed to be surrounded by LAMP1. This colocalization of overexpressing TNF-α and LAMP1 can be resulted from missorted overexpressing LAMP1; as such, TNF-α–LAMP1 colocalization was never observed in endogenous conditions. Nevertheless, we took advantage of those colocalized TNF-α–LAMP1 vesicles to characterize simultaneous release of TNF-α and LAMP1. We found that in the case of simultaneous release, the intensity of LAMP1 fluorescence did not increase after TNF-α release (Fig. 3G, 3H). Therefore, we prove that the sequential releases shown in Fig. 3E, 3F hold true, which further supports our conclusion that TNF-α$^+$ vesicles and LAMP$^+$ endocytic organelles are tethered.

Tethering between CytVs and endocytic organelles is mediated by Vti1b

To determine the molecular basis mediating the tethering between CytVs and lysosomes, we put our focus on Vti1b, a SNARE protein necessary for the juxtaposition of LG and CD3$^+$ endosomes in CD8$^+$ T cells (16). We first used modified siRNA to downregulate endogenous Vti1b in primary human CD4$^+$ T cells. We show that expression of Vti1b in CD4$^+$ T cells was downregulated by modified siRNA to <40% at both mRNA and protein levels (Fig. 4A–C). Immunostaining shows that in Vti1b-downregulated CD4$^+$ cells, the fraction of TNF-α$^+$ vesicles tethered with lysosomes (LAMP1$^+$) was significantly reduced (Fig. 4D, 4E). The total numbers of TNF-α$^+$ or LAMP1$^+$ vesicles remained unchanged (Fig. 4F). These experiments show that Vti1b is involved in tethering TNF-α$^+$ vesicles to lysosomes and that TNF-α–lysosome tethering does not affect the number of TNF-α$^+$ vesicles and lysosomes. We further examined whether blockage of Vti1b function could affect TNF-α release. Because Vti1b siRNA is not fluorescently labeled, to identify transfected T cells, we overexpressed the cytosolic fragment of Vti1b 1–207 to block the interaction of Vti1b with its cognate partners (35). We examined the secretion of TNF-α by TIRF microscopy. The results show that the cytosolic fragment of Vti1b 1–207 significantly diminished the fraction of the T cells that could release TNF-α (Fig. 4G) as well as the fusion events in each TNF-α–secreting cell (Fig. 4H). This result indicates that Vti1b-regulated LAMP1 tethering is also involved in TNF-α secretion.

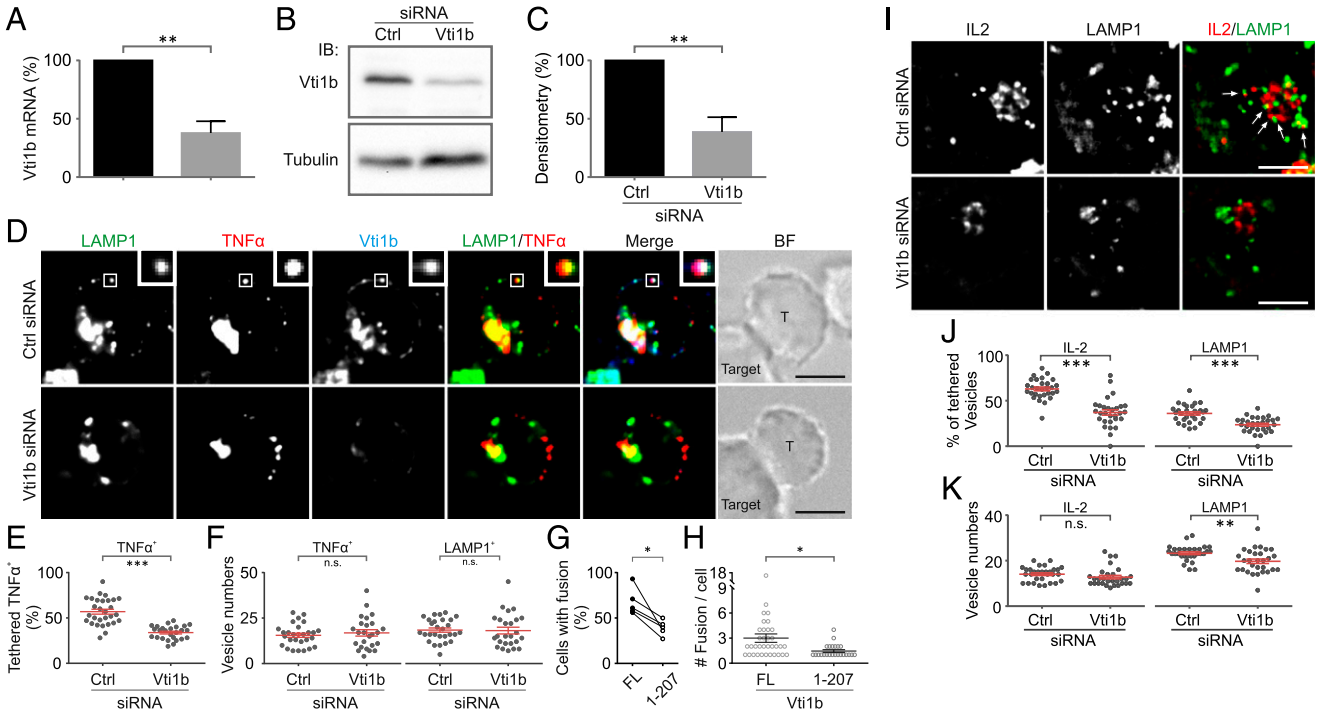

FIGURE 4. CytV–endocytic organelle tethering is Vti1b dependent. (**A**–**C**) Downregulation of Vti1b in T cells. Primary human $CD4^+$ T cells were stimulated with anti-CD3/anti-CD28 Ab-coated beads. Then, modified siRNA against Vti1b or control (Ctrl) siRNA were introduced into the cells. The cells were used for analysis 36 h after transfection. The mRNA level of Vti1b was determined using quantitative RT-PCR ($n = 3$ independent experiments with duplicates for each condition) in (A). TBP was applied as the reference gene. The protein level of Vti1b was determined using Western blotting with γ-tubulin as the internal control as shown in (B). Quantification of (B) is shown in (C) ($n = 3$ independent experiments). (**D**) Tethering between TNF-α^+ and $LAMP1^+$ vesicles is decreased by Vti1b downregulation. Stimulated primary human $CD4^+$ T cells were conjugated with target cells (SEA/SEB-pulsed Raji cells) at 37°C for 60 min and then fixed. Quantification of tethered TNF-α fraction as well as the total vesicle numbers of TNF-α^+ and $LAMP1^+$ vesicles (30 cells from three independent experiments) are shown in (**E**) and (**F**). (**G** and **H**) Overexpression of Vti1b 1–207 reduces TNF-α release. Stimulated primary human $CD4^+$ T cells transiently overexpressed mCherry-TNF-α with Vti1b FL-TFP or Vti1b 1-207-TFP were settled on anti-CD3/anti-CD28 Ab-coated coverslips. Movement and release of vesicles at the IS at 37°C were visualized by TIRF microscopy. The percentage of $CD4^+$ T cells that could release TNF-α is shown in (G). The number of TNF-α released in each cell is shown in (H). Results are from five independent experiments. (**I**–**K**) Tethering between IL-2 and LAMP1 is decreased by Vti1b downregulation. Stimulated primary human $CD4^+$ T cells were settled on anti-CD3/anti-CD28 Ab-coated coverslips at 37°C for 150 min before fixation. Endogenous IL-2 and LAMP1 were stained. The IS planes are shown, whereby IL-2/LAMP1 pairs are highlighted by the arrowheads. Percentage of tethered IL-2^+ vesicles and the vesicle numbers from three independent experiments are shown in (J) and (K). All samples were scanned with deconvolution microscopy with a ×63 objective. Scale bar, 5 μm. *$p < 0.05$, **$p < 0.01$, ***$p < 0.001$.

Similarly, the level of IL-2–lysosome tethering is also decreased significantly by downregulation of Vti1b (Fig. 4I, 4J). The number of IL-2^+ vesicles remained unchanged, whereas the number of $LAMP1^+$ vesicles was slightly reduced (Fig. 4K), which cannot be fully attributed to the substantial reduction in the level of IL-2–lysosome tethering by Vti1b downregulation. Thus, we conclude that tethering between CytVs and lysosomes is mediated by Vti1b.

Next, we looked for the interaction partner of Vti1b to regulate tethering. We focused on EpsinR because it has been shown to bind Vti1b and regulate the sorting of Vti1b (23). Using co-IP, we confirmed that two point mutants of human Vti1b, namely Vti1b-F73S and Vti1b-E12A, were not able to bind endogenous EpsinR as their WT counterpart Vti1b-WT (Fig. 5A), which is in good agreement with the previous report (23). Overexpression of Vti1b-F73S or Vti1b-E12A in primary $CD4^+$ T cells substantially reduced TNF-α–lysosome tethering (Fig. 5B, 5C) without affecting the total number of TNF-α^+ vesicles or lysosomes (Fig. 5D). We noticed that the overexpressed Vti1b is predominantly distributed on the plasma membrane, which might be due to the redundancy introduced by overexpression.

Our next question is whether these two point mutants of Vti1b (F73S and E12A) may interfere with the interaction between Vti1b and its cognate SNARE proteins. To this end, because it is very difficult to get a large enough number of primary T cells required to perform co-IP for all SNARE partners of Vti1b, we sought assistance from molecular modeling. We tested three computational tools, MAESTRO, ROSETTA, and BeAtMuSiC (36), based on structural data on the Vti1b/EpsinR complex. BeAtMuSiC (31) was determined as a suitable tool as it predicts seven out of eight residues that were previously experimentally determined to be important for the formation of this complex (Supplemental Table I). Furthermore, BeAtMuSiC suggests that F73 and E12 are not involved in Vti1b binding with its cognate SNARE proteins Syntaxin7, Syntaxin8, and VAMP8/Endobrevin (Supplemental Table II). Therefore, Vti1b F73S and Vti1b E12A appear to specifically block interaction between Vti1b and EpsinR without affecting the binding of Vti1b to its cognate SNARE partners. We therefore conclude that the interaction between Vti1b and EpsinR is required for CytV–lysosome tethering.

Lysosome tethering determines the direction of CytV transport

One important question is whether lysosome tethering contributes in any way to the distinct destination of TNF-α^+ and IL-2^+ vesicles, and if yes, how. To address this question, we designed experiments to analyze the localization of tethered versus untethered TNF-α^+ and IL-2^+ vesicles. For this analysis, the whole cell was divided into two different segments along the z-direction. As shown in Fig. 6A, the segment encompassing one fourth of the cell's

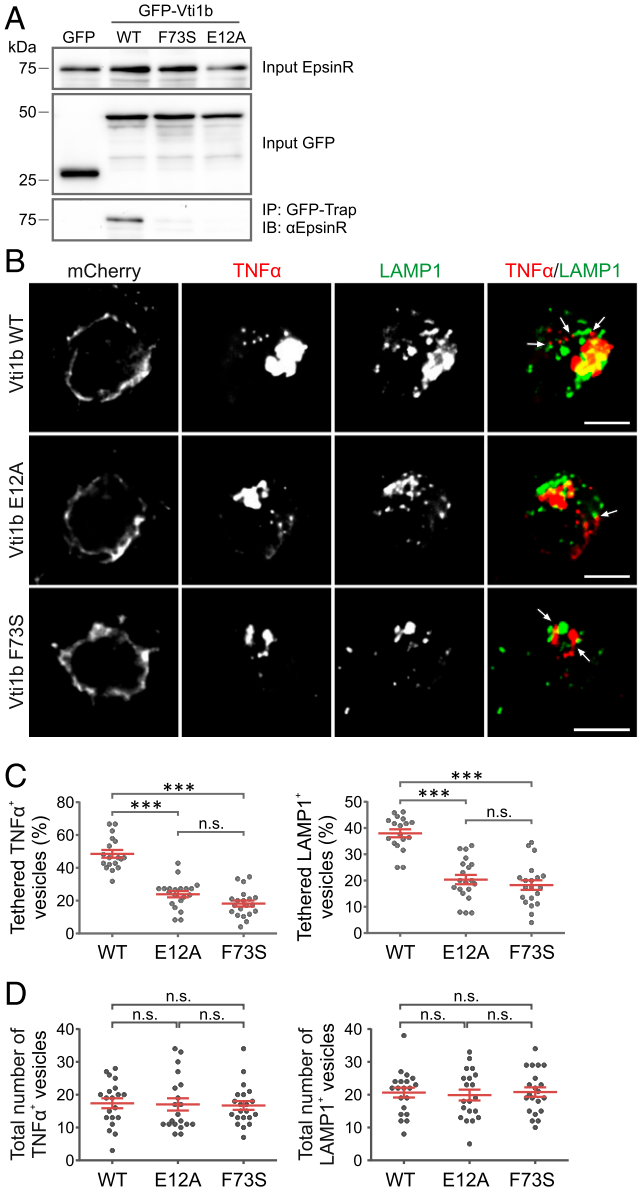

FIGURE 5. Interaction between Vti1b and EpsinR is required for CytV–endocytic organelle tethering. (**A**) Point mutants E12A and F73S of Vti1b abolish the interaction with EpsinR. GFP-tagged Vti1b WT, F73S, E12A, and GFP control vector were transiently transfected in HEK293T cells. Cells were lysed 24 h after transfection for co-IP. (**B**) Point mutants E12A and F73S of Vti1b substantially reduce tethering between TNF-α and LAMP1. Fluorescent protein mCherry-tagged Vti1b WT, F73S, or E12A were transiently overexpressed in primary human $CD4^+$ T cells. Twenty-four hours after transfection, T cells were settled on anti-CD3/anti-CD28 Ab-coated coverslips for 60 min followed by staining of endogenous TNF-α and LAMP1. The samples were scanned with deconvolution microscopy with a ×63 objective. A few examples of TNF-α–LAMP1 pairs are highlighted by arrowheads. Scale bar, 5 μm. Quantification of tethering probability and numbers of $TNF\text{-}\alpha^+$ and $LAMP1^+$ vesicles are shown in (**C**) and (**D**), respectively. All results are from three independent experiments. $***p < 0.001$

diameter close to the coverslip was defined as the IS area, and the rest of the cell was defined as the distal area. The analysis shows that the majority of lysosome-tethered TNF-α $^+$ vesicles were in the distal area, whereas the majority of untethered $TNF\text{-}\alpha^+$ vesicles were close to the IS (Fig. 6B, 6C). Conversely, the majority of lysosome-tethered IL-2 were enriched at the IS, whereas the majority of untethered IL-2 were in the distal area (Fig. 6B, 6D). These data suggest that by tethering to lysosomes, CytVs can be delivered to their desired destinations for both polarized and multidirectional localization.

The next question is whether the same $LAMP1^+$ organelle can tether with both TNF-α $^+$ and $IL\text{-}2^+$ vesicles. To address this question, we stained endogenous TNF-α, IL-2, and LAMP1 simultaneously in the same T cells. Quantifications shows that for both time points (90 and 120 min), the fractions of $LAMP1^+$ vesicles tethered with $IL\text{-}2^+$ or $TNF\text{-}\alpha^+$ vesicles were comparable (Fig. 6E, IL-2 versus TNF-α). We also observed that only occasionally, the same $LAMP1^+$ vesicles could tether with both $IL\text{-}2^+$ and $TNF\text{-}\alpha^+$ vesicles (Fig. 6F, IL-2 and TNF-α). Moreover, the numbers of $IL\text{-}2^+$ or $TNF\text{-}\alpha^+$ vesicles that tethered with LAMP1 also confirm that the majority of $TNF\text{-}\alpha^+$ and $IL\text{-}2^+$ vesicles do not share the same $LAMP1^+$ organelles (Fig. 6F).

Proportion of endocytic organelle-tethered CytVs modulates transport mode of CytVs

Subsequently, we investigated how lysosome tethering regulates the two modes of distribution. The direction of cargo transport is primarily defined by the attached motor proteins, namely plus and minus end directed microtubule motor proteins kinesin and dynein. There are more than 40 members of the kinesin superfamily (37). Specifically, blocking the function of several kinesin isoforms simultaneously either by pharmaceutical intervention or by small interference RNA in primary human T cells is experimentally very challenging, if not impossible. Therefore, we used mathematical models to understand how tethering could regulate these two modes of cytokine transport. First, we quantified the experimental observations by the introduction of various probabilities for untethered (index 0) and tethered (index t) vesicles. The probabilities for dynein and kinesins being attached to tethered and untethered TNF-α or IL-2 vesicles and the probabilities for untethered and tethered $TNF\text{-}\alpha^+$ or $IL\text{-}2^+$ vesicles to be located at the IS or distal to it were extracted from the experimental data (Figs. 6, 7) and are listed in Supplemental Table III. Based on these results, we analyzed the interrelation between lysosome tethering and location probabilities (close to or away from the IS) for $TNF\text{-}\alpha^+$ and $IL\text{-}2^+$ vesicles, respectively.

As shown in Eq. 1, the probability for CytV to be located at the IS (p_{IS}^{total}) is the sum of the probabilities of tethered and untethered CytV that are located at the IS:

$$p_{IS}^{total} = p^{tethering} \cdot p_{IS}^{t} + (1 - p^{tethering}) \cdot p_{IS}^{0} \tag{1}$$

The probabilities of tethered and untethered CytV that are located at the IS (p_{IS}^{t} and p_{IS}^{0}) were experimentally determined. For TNF-α, p_{IS}^{t}=0.3 (p_{Distal}^{t}=0.7), and p_{IS}^{0} =0.6 (p_{Distal}^{0}=0.4). For IL-2, p_{IS}^{0}=0.4 (p_{Distal}^{0}=0.6), and p_{IS}^{t} = 0.8 (p_{Distal}^{t}=0.2). Therefore, for TNF-α and IL-2, the correlation between p_{IS}^{total} and $p^{thethering}$ is opposite, as elaborated in Eqs. 2 and 3:

$$\begin{aligned} p_{IS}^{total\ \ TNF\alpha} &= p_{Tethering}^{TNF\alpha} \cdot 0.3 + (1 - p_{Tethering}^{TNF\alpha}) \cdot 0.6 \\ &= 0.6 - 0.3 \cdot p_{Tethering}^{TNF\alpha} \end{aligned} \tag{2}$$

$$\begin{aligned} p_{IS}^{total\ \ IL-2} &= p_{Tethering}^{IL-2} \cdot 0.8 + (1 - p_{Tethering}^{IL-2}) \cdot 0.4 \\ &= 0.4 + 0.4 \cdot p_{Tethering}^{IL-2} \end{aligned} \tag{3}$$

The fraction of TNF-α accumulated at the IS is negatively correlated with the probability of TNF-α tethering with lysosomes ($p_{Tethering}^{TNF\alpha}$) (Fig. 8A), whereas for IL-2, the higher the tethering rate, the higher the propensity to stay at the IS (Fig. 8B). For the vesicle distribution to be considered to be multidirectional, at the most, half of the vesicles may be found near the IS. Thus, a line may be drawn when

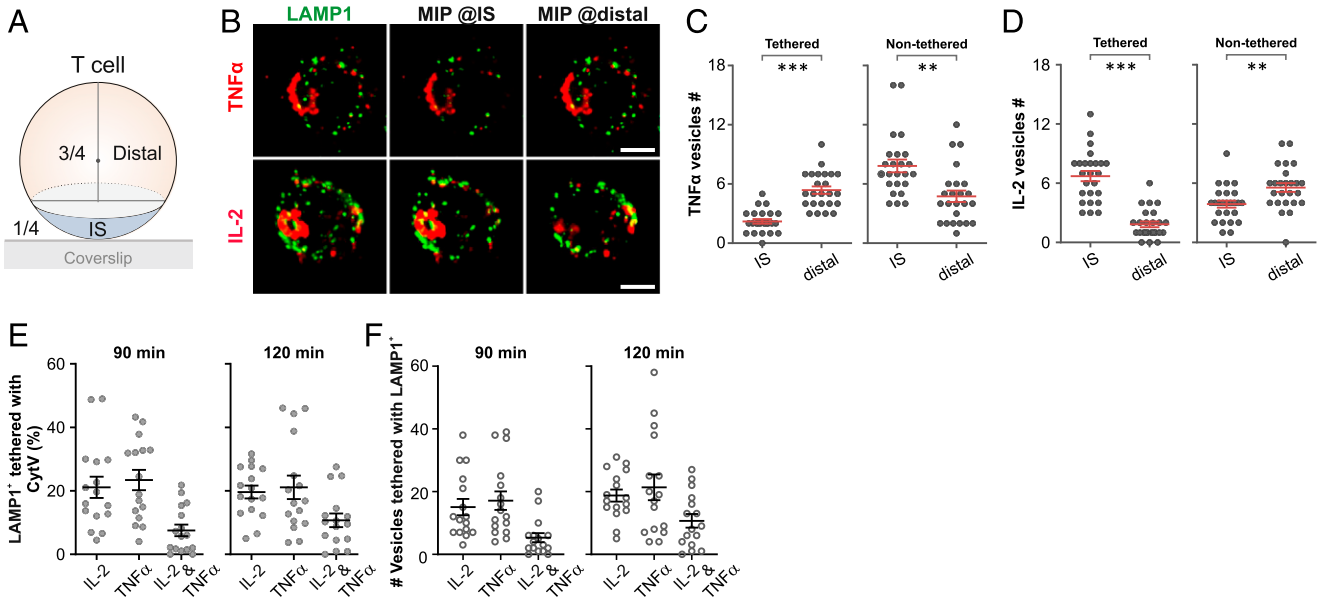

FIGURE 6. Tethering to LAMP1$^+$ organelles determines the transport direction of cytokines. CD4$^+$ T cells were restimulated with anti-CD3/anti-CD28 Ab-coated beads for 120 min (**B**–**D**) or 90 or 120 min (**E** and **F**). After bead removal, the T cells were fixed and stained with corresponding Abs. (**A**) Distribution of vesicles in the vicinity to the IS (@IS) or away from the IS (@distal). (B–D) Tethering is involved in directional transport for both TNF-α$^+$ and IL-2$^+$ vesicles. Anti–TNF-α or anti–IL-2 and anti-LAMP1 Abs were used. Z-stacks were taken with a z-step size of 0.2 μm by deconvolution microscopy with a ×63 objective. Distribution for TNF-α$^+$ and IL-2$^+$ vesicles at the IS or distal areas was shown in (B). Analyses of distribution of TNF-α$^+$ or IL-2$^+$ vesicles are shown in (C) and (D). Scale bar, 5 μm. Results were from three independent experiments (24 cells). (E and F) Tethering of LAMP1 with CytVs in the same T cells. Endogenous TNF-α, IL-2, and LAMP1 were stained after fixation. The fractions of LAMP1 tethered with IL-2, TNF-α, or IL-2 and TNF-α are shown in (E). The numbers of CytVs tethered with LAMP1$^+$ organelles are shown in (F). Results were from two independent experiments (16 cells). $^{**}p < 0.01$, $^{***}p < 0.001$. MIP, maximum intensity projection.

p_{IS}^{total} equals 0.5, which defines the boundary between polarized versus multidirectional transport. Consequently, the tethering probability of TNF-α must be larger than 0.33 (Fig. 8A, gray area) for multidirectional transport to occur. For IL-2, to achieve a polarized pattern ($p_{IS}^{total\ \ IL-2} \geq 0.5$), the tethering probability of IL-2 needs only to be larger than 25% ($p^{tethered} \geq 0.25$,Fig. 8B, gray area). Thus, we conclude that tethering with lysosomes facilitates that TNF-α and IL-2 achieve their desired destinations.

Next, we analyzed the impact of tethering-regulated motor protein recruitment on CytV transport. For TNF-α, we assume that the kinesin outperforms dynein if both motor proteins are recruited on the same vesicle, which is also supported by the fact that the stall force of kinesin is much higher than the stall force of dynein (38). We also introduced a dynein inhibition probability on TNF-α vesicles and denoted it as p_{dyn}^{inh}. Then, the probability for untethered TNF-α to be at the IS, p_{IS}^{0}, is:

$$p_{IS}^{0} = \left(1 - p_{dyn}^{0}\right)\left(1 - p_{kin}^{0}\right) + \left(1 - p_{dyn}^{inh}\right)p_{dyn}^{0}\left(1 - p_{kin}^{0}\right) + p_{dyn}^{inh}p_{dyn}^{0}\left(1 - p_{kin}^{0}\right)$$

where the first term on the right-hand side is the probability for having neither dynein nor kinesin on untethered TNF-α vesicles, in which case the vesicle stays close to the microtubule organizing center (MTOC) and thus at the IS. The second term is the probability that a vesicle contains dynein, that this dynein is not inhibited, and that the vesicle does not contain kinesin, in which case it would also stay near the MTOC/IS. The third term is the probability that dynein is present but is inhibited, yet kinesin is also absent, in which case the vesicle would still remain near the IS. This equation can be simplified to the following:

$$p_{IS}^{0} = 1 - p_{kin}^{0} = 0.8$$

Notably, neither p_{dyn}^{0} nor p_{dyn}^{inh} play a role in determination of TNF-α distribution, only the presence of kinesin. In other words, for an untethered TNF-α$^+$ vesicle to remain at the IS, kinesin has to be absent, and for their transport away from the IS, kinesin must be present. Because the quantification of our experimental observation about the number of vesicles being located at the IS or at the distal area (dist) shows that p_{IS}^{0} is around 0.6 (and hence $p_{dist}^{0} = 0.4$), there should be other kinesins (e.g., kinesin-3 [denoted as *kin-x*]) involved besides kinesin-1, so that we have

$$p_{kin} = p_{kin-1} + p_{kin-x}$$

Because we measured the probability of finding kinesin on untethered vesicles to be $p_{kin-1}^{0} = 0.2$ and $p_{dist}^{0} = p_{kin}^{0} = 0.4$, the probability for other kinesins, p_{kin-x}^{0}, should be around 0.2. In comparison, on tethered TNF-α$^+$ vesicles, the probability to have dynein or kinesin is $p_{dyn}^{t} = 0.4$ and $p_{kin}^{t} = 0.5$, respectively. The resulting probability to find tethered TNF-α$^+$ vesicles at the IS are then:

$$p_{IS}^{t} = 1 - p_{kin}^{t} = 0.5 \quad (4)$$

Experimentally, we observed $p_{IS}^{t} \approx 0.3$, which is smaller than the value predicted from Eq. 4 based on the measurement of kinesin-1. Therefore, we postulate again the presence of other kinesins on tethered TNF-α$^+$ vesicles, such that

$$p_{kin}^{t} = p_{kin-1}^{t} + p_{kin-x}^{t}$$

Therefore, we get the following:

$$p_{IS}^{t} = 0.5 - p_{kin-x}^{t}$$

To obtain $p_{IS}^{t} \approx 0.3$, one must again have $p_{kin-x}^{t} = 0.2$, which is similar to p_{kin-x}^{0}, the probability for other kinesins on untethered TNF-α$^+$ vesicles.

To analyze how the recruitment of motor proteins and tethering contributes to the final distribution of IL-2, we first assumed that kinesin outperforms dynein, as for TNF-α. Thus:

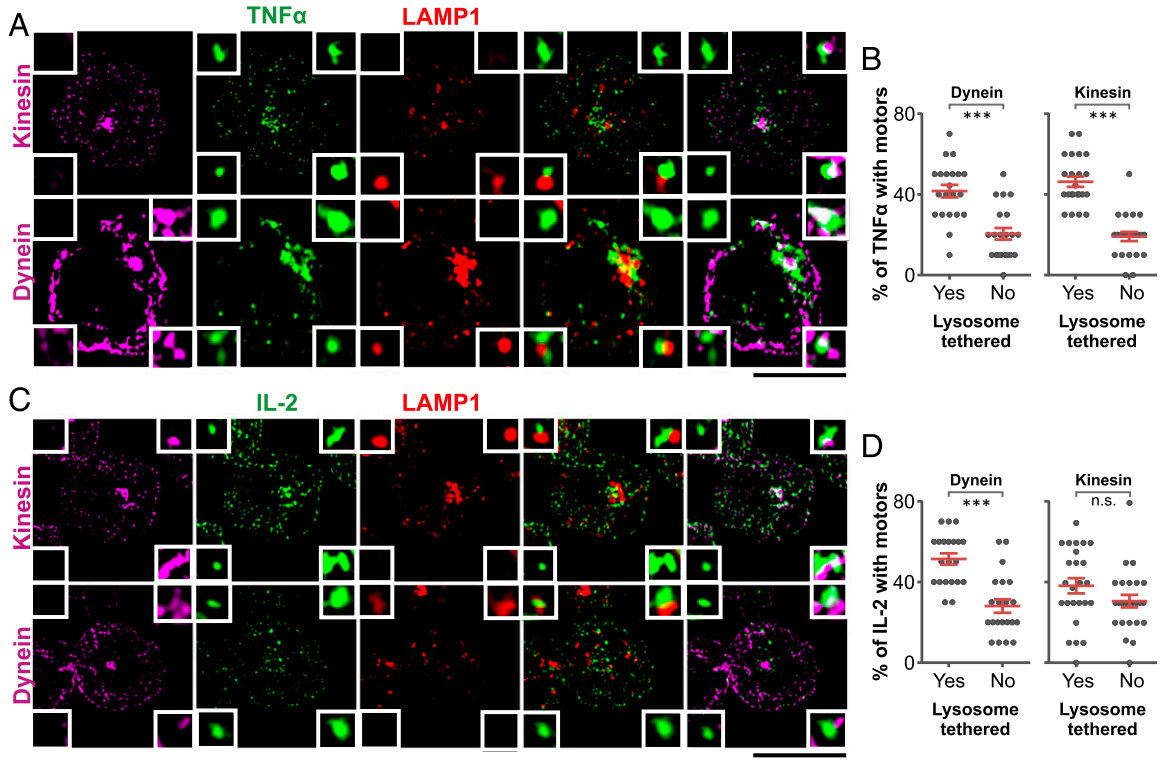

FIGURE 7. Association of dynein and kinesin on TNF-α^+ and IL-2^+ vesicles. Anti–TNF-α (**A**) or anti–IL-2 (**C**, green), anti-LAMP1 (red), and anti-kinesin or anti-dynein (magenta) Abs were used. Images were acquired by SIM using a ×63 objective. The association between TNF-α and motor proteins was quantified in (**B**). Ten tethered or untethered TNF-α^+ vesicles were randomly selected from each cell [23 cells from three independent experiments (B)]. Ten tethered or untethered IL-2^+ vesicles were randomly selected from each cell (25 cells from three independent experiments), and the association between IL-2 and motor proteins is shown in (**D**). Scale bar, 5 μm. ***$p < 0.001$

$$p^0_{IS} = 1 - p^0_{kin} = 0.4(\text{exp. determined})$$

$$p^t_{IS} = 1 - p^t_{kin} = 0.8(\text{exp. determined})$$

With this, the probability for kinesin on untethered and tethered IL-2 should be $p^0_{kin} = 0.6$ and $p^t_{kin} = 0.2$. The latter is incompatible with our experimental result $p^t_{kin-1} = 0.4$. Therefore, the assumption that kinesin always outperforms dynein must be false for IL-2. We can postulate two alternative scenarios that could help explain this discrepancy.

First, we could assume conversely that dynein outcompetes kinesin (Mechanism 1) (e.g., by the number of dyneins being much larger than the number of kinesins). Then, we obtain

$$p^t_{IS} = \left(1 - p^t_{kin}\right) + p^t_{dyn}p^t_{kin}$$

$$p^0_{IS} = \left(1 - p^0_{kin}\right) + p^0_{dyn}p^0_{kin}$$

where the first term on the right-hand side is the probability for the absence of kinesin, and the second term is the probability that both dynein and kinesin are present, in which case dynein wins. By inserting the experimental values for p^0_{dyn} (0.3) and p^t_{dyn} (0.5), we get:

$$p^t_{IS} = 1 - 0.5p^t_{kin} \quad (5)$$

$$p^0_{IS} = 1 - 0.7p^0_{kin} \quad (6)$$

Fig. 8C shows the dependency of IS enrichment (P_{IS}) on the attachment of kinesin (P_{kin}), as given by Eqs. 5 and 6. One can see that the probability to find IL-2 at the IS is negatively correlated with their attached kinesin (Fig. 8C), which is expected. In addition, one can see that by increasing the deposition of dynein, tethering of IL-2^+ vesicles increases the propensity of finding IL-2^+ vesicles at the IS. For the probability of untethered IL-2 being found at the IS, p^0_{IS}, to be around 0.4 (experimental observation), the required p^0_{kin} should be 0.86 (Fig. 8C, blue dashed lines), which again implies additional kinesins are involved in the case of untethered IL-2^+ vesicles. For tethered IL-2^+ vesicles, p^t_{IS} = 0.8, and the corresponding p^t_{kin} should be 0.4 (Fig. 8C, red dashed lines), which agrees with the experimentally determined p^t_{kin-1} (Fig. 7, Supplemental Table III).

In a second scenario, we assumed that kinesin is inhibited on IL-2 (Mechanism 2) with probability p^{inh}_{kin}. Then, one has

$$p^0_{IS} = \left(1 - p^0_{kin}\right) + p^{inh}_{kin}p^0_{kin} = 0.4(\text{exp. determined}) \quad (7)$$

$$p^t_{IS} = \left(1 - p^t_{kin}\right) + p^{inh}_{kin}p^t_{kin} = 0.8(\text{exp. determined}) \quad (8)$$

where the first term on the right-hand side is the probability that kinesin is absent on IL-2^+ vesicles, in which case the vesicles stay close to the MTOC and thus at the IS. The second term is the probability that kinesins are present but inhibited. By plotting P_{IS} as a function of p^{inh}_{kin}, we find that with Mechanism 2, the probability of IL-2^+ vesicles to be enriched at the IS is positively correlated with and proportional to p^{inh}_{kin} (Fig. 8D, left panel) and independent of dynein attachment (Eqs. 7, 8). To reproduce the experimentally determined values for p^0_{IS} (0.4) and p^t_{IS} (0.8), the kinesin inhibition probability p^{inh}_{kin} on tethered IL-2 must be substantially higher compared with untethered if P_{kin} is identical for tethered and untethered IL-2. If, in contrast, p^{inh}_{kin} is identical in both cases, the recruitment of kinesin on tethered IL-2 should be considerably lower than untethered IL-2 (Fig. 8D, right panel).

The above-mentioned Mechanisms 1 and 2 could also be combined (kinesin inhibition and outperformance of dynein over uninhibited kinesin, Mechanism 3). Then, one has the following:

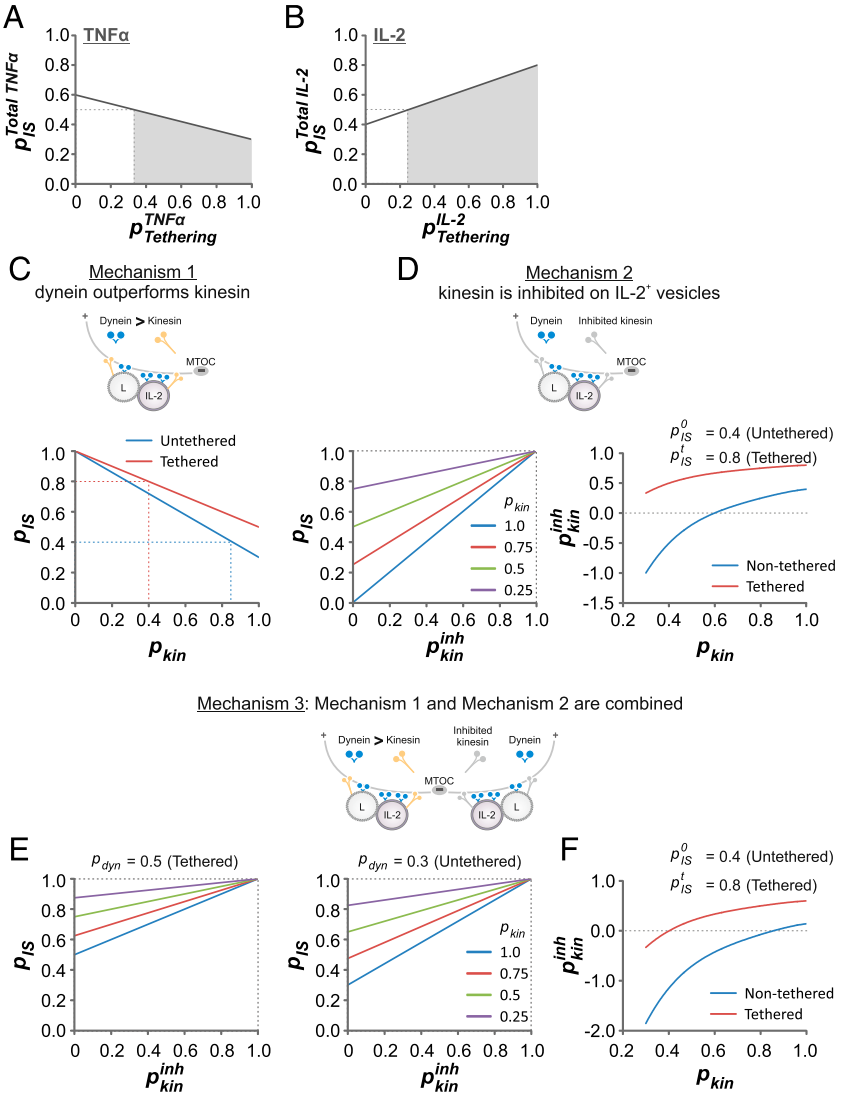

FIGURE 8. Mathematical models for endocytic organelle tethering directed cytokine transport. (**A** and **B**) The fractions of CytVs accumulated at the IS and the proportion of lysosome-tethered CytVs are negatively correlated for TNF-α$^+$ vesicles and positively correlated for IL-2$^+$ vesicles. The gray area marks the fraction of tethered vesicles required for TNF-α to have a multidirectional distribution (A) or for IL-2 to have an IS-polarized distribution (B). (**C**) The correlation of the probability to find IL-2 vesicles at the IS (P_{IS}) with the attached kinesins (P_{kin}) when dynein outperforms kinesin (Mechanism 1). The dashed lines show the required P_{kin} to meet experimentally determined P_{IS}. (**D**) Distribution of IL-2 when kinesin is inhibited (Mechanism 2). The probability of kinesin inhibition (p_{kin}^{inh}) was set to 0, 0.5, 0.75, and 1 for Eqs. 6 and 7 (left panel). To obtain the experimentally determined p_{IS}^0 (0.4) and p_{IS}^t (0.8), the correlation between p_{kin}^{inh} and P_{kin} is shown in the right panel. (**E**) Distribution of IL-2 with the assumptions that kinesin is partially inhibited and that dynein outperforms uninhibited kinesin (Mechanism 3). (**F**) The correlation between p_{kin}^{inh} and P_{kin} to obtain the experimentally determined p_{IS}^0 (0.4) and p_{IS}^t (0.8) with Mechanism 3.

$$p_{IS}^t = \left(1 - p_{kin}^t\right) + p_{dyn}^t\left(1 - p_{kin}^{inh}\right)\ p_{kin}^t + p_{kin}^{inh} p_{kin}^t$$

$$p_{IS}^0 = \left(1 - p_{kin}^0\right) + p_{dyn}^0\left(1 - p_{kin}^{inh}\right)\ p_{kin}^0 + p_{kin}^{inh} p_{kin}^0$$

In this combined case, the probability of IS enrichment of IL-2$^+$ vesicles is also positively correlated with and proportional to p_{kin}^{inh} and, in addition, is also dependent on dynein attachment (Fig. 8E). To obtain the experimentally determined values for p_{IS}^0 (0.4) and p_{IS}^t (0.8), the dependency of p_{kin}^{inh} on P_{kin} is similar as for Mechanism 2, namely identical P_{kin} requires higher p_{kin}^{inh} on tethered compared with untethered IL-2$^+$ vesicles, and identical p_{kin}^{inh} would imply a lower level of total kinesin on tethered as compared with untethered IL-2$^+$ vesicles (Fig. 8F). Notably, the range of P_{kin} to obtain a positive value of p_{kin}^{inh} from Mechanism 3 is narrower than Mechanism 2. In addition, Mechanism 2 and Mechanism 3 predict higher $p_{kin}^{inh}$and/or lower P_{kin} on tethered IL-2$^+$ vesicles, suggesting that tethering is correlated with removing or detaching kinesins on tethered IL-2$^+$ vesicles.

Discussion

In this work, using various microscopic approaches including high-resolution microscopy, live-cell imaging, TIRF, and CLEM, we prove that CytV physically tether with endocytic organelles, namely late endosomes/lysosomes. In this study, we used two methods for IS formation, Raji cells and anti-CD3/anti-CD28Ab-coated coverslips. Raji–CD4–T cell model represents a "real" IS, whereas the coated coverslips are optimal for high-resolution TIRF microscopy. More particularly, with Ab-coated coverslips, the position of the IS can be much more precisely determined. Remarkably, to observe the details of vesicle movement and release at the IS, TIRF is required, which can be conducted only with a coverslip-based experimental setup. To confirm tandem transportation of CytV–LAMP1 pairs, we used TIRF and LCSM. When using TIRF, EGFP and mCherry were illuminated one after the other with a lag of 73 ms; colocalized CytV–LAMP1 could look like being tethered when moving fast. Fortunately, this possibility is excluded by the tandem transportation of tethered CytV–LAMP1 pairs visualized by LCSM, whereby EGFP and mCherry were illuminated simultaneously, confirming that tandem transport of tethered CytV–LAMP1 pairs does occur.

Tethering between organelles/vesicles is a stable state, which does not result in fusion or coalescence of the tethered entities. Interestingly, prior to fusion events, the vesicle/organelle membrane and the target membrane are also positioned in close vicinity and physically connected. This stage is termed "docking," which shares many common characteristics with canonical interorganelle tethering. Compelling evidence shows that membrane fusion mediating proteins can also serve as major players to initiate and maintain contact sites for tethered organelles/vesicles. One example

is Sec22b, a SNARE protein, which mediates ER–plasma membrane tethering by forming an incomplete, nonfusogenic SNARE complex with syntaxin 1 on the plasma membrane (19). Another good example is Vps39, a component of the homotypic fusion and protein sorting complex, which is involved in tethering vacuoles with mitochondria (39–41). Both Sec22b and Vps39 have well-established roles in mediating vesicular fusion (42–45), indicating that mediating fusion and tethering are not mutually exclusive.

Proteins mediating tethering of opposing membranes can be classified into "principal tether" and "auxiliary tether." The difference is whether the protein(s) are necessary and sufficient for the formation and/or maintenance of contact sites independent of other components (10). The absence of principal tethers leads to a reduction of tethering. In this work, we reveal that downregulation of Vti1b leads to a reduction in CytV–endocytic organelle tethering in primary human $CD4^+$ T cells and that the interaction between Vti1b and its interaction partner EpsinR is essential for the formation of MCSs between CytV and late endosomes/lysosomes. These findings suggest that Vti1b and EpsinR play a key role in forming and/or maintaining endocytic organelle-related interorganelle tethering in T cells. Whether Vti1b and EpsinR are located on two opposing membranes and serve as primary tethers is still not known. In theory, Vti1b could also be first sorted to the corresponding vesicles via EpsinR (23) and then mediate CytV–lysosome tethering by forming a nonfusogenic SNARE complex with its cognate SNARE partners. To identify which of the above-mentioned possibilities is true requires further investigation. By Vti1b downregulation, the numbers of $LAMP1^+$ vesicles were unchanged in Fig. 4F but slightly reduced in Fig. 4J. This reduction is so small that we suspect it might be introduced by the variation among donors. Vti1b is not thought to be involved in regulating the generation of CytVs or lysosomes.

Interorganelle tethering is believed to be a major mechanism for communication between many, possibly all, organelles (10). The roles of interorganelle tethering identified so far mainly concern the exchange of small molecules between tethered organelles/vesicles at MCSs, for example lipids, ions, and glucose (13, 19, 46, 47). In this work, we prove that in primary human $CD4^+$ T cells, CytVs tether with lysosomes/endosomes by forming a physically connected MCS. By tethering with lysosome, IL-2^+ vesicles are directed to the IS, whereas TNF-α^+ vesicles are multidirectionally targeted.

Mathematical models are used widely to illustrate complex biological processes including vesicular transportation (48–51). Our mathematical models suggest that this distinct preference in transportation is likely linked to the change in the attachment of motor proteins, namely dynein and kinesin, by late endosome/lysosome tethering. This possibility is supported by the evidence that ER endosome MCSs regulate the trafficking of endosomes by providing a platform to transfer kinesin-1 from ER to endosomes (52, 53).

The organelles that CytVs tethered with are shown in this work to be Rab7 positive. Rab7 is reported to be involved in ER–late endosome tethering (54). Intriguingly, Rab7 is responsible for recruiting kinesin-1 from ER to endosomes at ER endosomal MCSs under conditions of low cholesterol, and in parallel, under conditions of high cholesterol, Rab7 is involved in attaching dynein to late endosomes via its interaction partner RILP (52, 53). A recent study reported that the Rab7 effector PLEKHM1 competes with SKIP to modulate the recruitment of kinesin (55). Thus, Rab7 could be involved in regulating the recruitment of dynein or kinesins onto tethered CytVs through MCSs, depending on the resident components on targeting CytVs. Other potential players, however, should not be excluded.

In this study, we formulated a model for the correlation of transport direction with LAMP1 tethering and with vesicle motor equipment based on the quantification of experimental observations. By counting the number of TNF-α^+ or IL-2^+ vesicles, untethered or tethered, that are equipped with dynein or kinesin, we determined the probabilities p^0_{dyn}, p^0_{kin}, p^t_{dyn}, and p^t_{kin}, and by counting the number of vesicles being located at the IS or at the distal area, we determined the probabilities p^0_{IS}, p^0_{dist}, p^t_{IS} and p^t_{dist}. One observes that for TNF-α^+ vesicles and for untethered IL-2^+ vesicles, the probability for kinesin-1 equipment (p_{kin}) is strictly related to the probability to be located distal (p_{dist}); in all three cases, the difference between p_{dist} and $p_{kin\text{-}1}$ is 0.2, which indicates the existence of another type of kinesin that has not been tested for. Moreover, one observes that for tethered IL-2^+ vesicles, the probability to be equipped with kinesin, ($p_{kin\text{-}1}$), is larger than the probability to be located at the distal area, p_{dist}, which indicates the existence of a mechanism that impedes kinesin action. Together, our model predicts that endocytic organelle tethering-regulated changes in the probabilities of kinesin and dynein attaching to TNF-α^+ or IL-2^+ vesicles can result in a multidirectional distribution for TNF-α^+ vesicles and an IS polarization for IL-2^+ vesicles. These results further support our conclusion that the multidirectional and polarized modes of cytokine transport in T cells are regulated by lysosome tethering, most likely by modulating the attachment of motor proteins to the CytVs.

Acknowledgments

We thank the Institute for Clinical Hemostaseology and Transfusion Medicine for providing donor blood; Carmen Hässig, Cora Hoxha, and Gertrud Schwär for excellent technical help; Jens Rettig (Saarland University) for mCherry-Rab5a,mCherry-Rab7a, and mCherry-Rab11a; Lei Lu (Nanyang Technological University) for LAMP1-EGFP and CD63-EGFP constructs; platform P1 Sonderforschungsbereich 894 for the use of SIM; Laura De Luca and Irina Nikonenko (Pôle Facultaire de Microscopie Electronique, Université de Genève) for help with EM; and Sandra Janku for careful and critical reading. We are grateful to Markus Hoth for constant support, inspiring discussions, and advice regarding the writing of this manuscript.

Disclosures

The authors have no financial conflicts of interest.

References

1. Kupfer, A., T. R. Mosmann, and H. Kupfer. 1991. Polarized expression of cytokines in cell conjugates of helper T cells and splenic B cells. *Proc. Natl. Acad. Sci. USA* 88: 775–779.
2. Kupfer, H., C. R. Monks, and A. Kupfer. 1994. Small splenic B cells that bind to antigen-specific T helper (Th) cells and face the site of cytokine production in the Th cells selectively proliferate: immunofluorescence microscopic studies of Th-B antigen-presenting cell interactions. *J. Exp. Med.* 179: 1507–1515.
3. Zhu, J., H. Yamane, and W. E. Paul. 2010. Differentiation of effector CD4 T cell populations. *Annu. Rev. Immunol.* 28: 445–489.
4. Taniuchi, I. 2018. CD4 helper and CD8 cytotoxic T cell differentiation. *Annu. Rev. Immunol.* 36: 579–601.
5. Smith, K. M., L. Pottage, E. R. Thomas, A. J. Leishman, T. N. Doig, D. Xu, F. Y. Liew, and P. Garside. 2000. Th1 and Th2 CD4+ T cells provide help for B cell clonal expansion and antibody synthesis in a similar manner in vivo. *J. Immunol.* 165: 3136–3144.
6. Martinez, F. O., and S. Gordon. 2014. The M1 and M2 paradigm of macrophage activation: time for reassessment. *F1000Prime Rep.* 6: 13.
7. Luckheeram, R. V., R. Zhou, A. D. Verma, and B. Xia. 2012. $CD4^+$ T cells: differentiation and functions. *Clin. Dev. Immunol.* 2012: 925135.
8. Huse, M., B. F. Lillemeier, M. S. Kuhns, D. S. Chen, and M. M. Davis. 2006. T cells use two directionally distinct pathways for cytokine secretion. *Nat. Immunol.* 7: 247–255.
9. Scorrano, L., M. A. De Matteis, S. Emr, F. Giordano, G. Hajnóczky, B. Kornmann, L. L. Lackner, T. P. Levine, L. Pellegrini, K. Reinisch, et al. 2019. Coming together to define membrane contact sites. *Nat. Commun.* 10: 1287.
10. Eisenberg-Bord, M., N. Shai, M. Schuldiner, and M. Bohnert. 2016. A tether is a tether is a tether: tethering at membrane contact sites. *Dev. Cell* 39: 395–409.
11. Quintana, A., M. Pasche, C. Junker, D. Al-Ansary, H. Rieger, C. Kummerow, L. Nuñez, C. Villalobos, P. Meraner, U. Becherer, et al. 2011. Calcium microdomains

at the immunological synapse: how ORAI channels, mitochondria and calcium pumps generate local calcium signals for efficient T-cell activation. *EMBO J.* 30: 3895–3912.
12. Wong, Y. C., D. Ysselstein, and D. Krainc. 2018. Mitochondria-lysosome contacts regulate mitochondrial fission via RAB7 GTP hydrolysis. *Nature* 554: 382–386.
13. Chu, B. B., Y. C. Liao, W. Qi, C. Xie, X. Du, J. Wang, H. Yang, H. H. Miao, B. L. Li, and B. L. Song. 2015. Cholesterol transport through lysosome-peroxisome membrane contacts. *Cell* 161: 291–306.
14. Höglinger, D., T. Burgoyne, E. Sanchez-Heras, P. Hartwig, A. Colaco, J. Newton, C. E. Futter, S. Spiegel, F. M. Platt, and E. R. Eden. 2019. NPC1 regulates ER contacts with endocytic organelles to mediate cholesterol egress. *Nat. Commun.* 10: 4276.
15. Liu, D., Y. T. Bryceson, T. Meckel, G. Vasiliver-Shamis, M. L. Dustin, and E. O. Long. 2009. Integrin-dependent organization and bidirectional vesicular traffic at cytotoxic immune synapses. *Immunity* 31: 99–109.
16. Qu, B., V. Pattu, C. Junker, E. C. Schwarz, S. S. Bhat, C. Kummerow, M. Marshall, U. Matti, F. Neumann, M. Pfreundschuh, et al. 2011. Docking of lytic granules at the immunological synapse in human CTL requires Vti1b-dependent pairing with CD3 endosomes. *J. Immunol.* 186: 6894–6904.
17. Stanley, A. C., and P. Lacy. 2010. Pathways for cytokine secretion. *Physiology (Bethesda)* 25: 218–229.
18. Ungar, D., and F. M. Hughson. 2003. SNARE protein structure and function. *Annu. Rev. Cell Dev. Biol.* 19: 493–517.
19. Petkovic, M., A. Jemaiel, F. Daste, C. G. Specht, I. Izeddin, D. Vorkel, J. M. Verbavatz, X. Darzacq, A. Triller, K. H. Pfenninger, et al. 2014. The SNARE Sec22b has a non-fusogenic function in plasma membrane expansion. *Nat. Cell Biol.* 16: 434–444.
20. Luzio, J. P., P. R. Pryor, and N. A. Bright. 2007. Lysosomes: fusion and function. *Nat. Rev. Mol. Cell Biol.* 8: 622–632.
21. Hirst, J., S. E. Miller, M. J. Taylor, G. F. von Mollard, and M. S. Robinson. 2004. EpsinR is an adaptor for the SNARE protein Vti1b. *Mol. Biol. Cell* 15: 5593–5602.
22. Chidambaram, S., N. Müllers, K. Wiederhold, V. Haucke, and G. F. von Mollard. 2004. Specific interaction between SNAREs and epsin N-terminal homology (ENTH) domains of epsin-related proteins in trans-Golgi network to endosome transport. *J. Biol. Chem.* 279: 4175–4179.
23. Miller, S. E., B. M. Collins, A. J. McCoy, M. S. Robinson, and D. J. Owen. 2007. A SNARE-adaptor interaction is a new mode of cargo recognition in clathrin-coated vesicles. *Nature* 450: 570–574.
24. Kummerow, C., E. C. Schwarz, B. Bufe, F. Zufall, M. Hoth, and B. Qu. 2014. A simple, economic, time-resolved killing assay. *Eur. J. Immunol.* 44: 1870–1872.
25. Gustafsson, M. G., L. Shao, P. M. Carlton, C. J. Wang, I. N. Golubovskaya, W. Z. Cande, D. A. Agard, and J. W. Sedat. 2008. Three-dimensional resolution doubling in wide-field fluorescence microscopy by structured illumination. *Biophys. J.* 94: 4957–4970.
26. Rosselin, M., P. Nunes-Hasler, and N. Demaurex. 2018. Ultrastructural characterization of flashing mitochondria. *Contact (Thousand Oaks)* 1: 1–14.
27. Nunes-Hasler, P., S. Maschalidi, C. Lippens, C. Castelbou, S. Bouvet, D. Guido, F. Bermont, E. Y. Bassoy, N. Page, D. Merkler, et al. 2017. STIM1 promotes migration, phagosomal maturation and antigen cross-presentation in dendritic cells. *Nat. Commun.* 8: 1852.
28. Berman, H. M., J. Westbrook, Z. Feng, G. Gilliland, T. N. Bhat, H. Weissig, I. N. Shindyalov, and P. E. Bourne. 2000. The protein Data Bank. *Nucleic Acids Res.* 28: 235–242.
29. Laimer, J., H. Hofer, M. Fritz, S. Wegenkittl, and P. Lackner. 2015. MAESTRO--multi agent stability prediction upon point mutations. *BMC Bioinformatics* 16: 116.
30. Kortemme, T., D. E. Kim, and D. Baker. 2004. Computational alanine scanning of protein-protein interfaces. *Sci. STKE* 2004: pl2.
31. Dehouck, Y., J. M. Kwasigroch, M. Rooman, and D. Gilis. 2013. BeAtMuSiC: prediction of changes in protein-protein binding affinity on mutations. *Nucleic Acids Res.* 41(W1): W333–W339.
32. Antonin, W., D. Fasshauer, S. Becker, R. Jahn, and T. R. Schneider. 2002. Crystal structure of the endosomal SNARE complex reveals common structural principles of all SNAREs. *Nat. Struct. Biol.* 9: 107–111.
33. Schrader, M., L. F. Godinho, J. L. Costello, and M. Islinger. 2015. The different facets of organelle interplay-an overview of organelle interactions. *Front. Cell Dev. Biol.* 3: 56.
34. Wang, L., C. Vasilev, D. P. Canniffe, L. R. Wilson, C. N. Hunter, and A. J. Cadby. 2012. Highly confined surface imaging by solid immersion total internal reflection fluorescence microscopy. *Opt. Express* 20: 3311–3324.
35. Murray, R. Z., F. G. Wylie, T. Khromykh, D. A. Hume, and J. L. Stow. 2005. Syntaxin 6 and Vti1b form a novel SNARE complex, which is up-regulated in activated macrophages to facilitate exocytosis of tumor necrosis Factor-alpha. *J. Biol. Chem.* 280: 10478–10483.
36. Gromiha, M. M., K. Yugandhar, and S. Jemimah. 2017. Protein-protein interactions: scoring schemes and binding affinity. *Curr. Opin. Struct. Biol.* 44: 31–38.
37. Hirokawa, N., Y. Noda, Y. Tanaka, and S. Niwa. 2009. Kinesin superfamily motor proteins and intracellular transport. *Nat. Rev. Mol. Cell Biol.* 10: 682–696.
38. Müller, M. J., S. Klumpp, and R. Lipowsky. 2008. Tug-of-war as a cooperative mechanism for bidirectional cargo transport by molecular motors. *Proc. Natl. Acad. Sci. USA* 105: 4609–4614.
39. Elbaz-Alon, Y., E. Rosenfeld-Gur, V. Shinder, A. H. Futerman, T. Geiger, and M. Schuldiner. 2014. A dynamic interface between vacuoles and mitochondria in yeast. *Dev. Cell* 30: 95–102.
40. Hönscher, C., M. Mari, K. Auffarth, M. Bohnert, J. Griffith, W. Geerts, M. van der Laan, M. Cabrera, F. Reggiori, and C. Ungermann. 2014. Cellular metabolism regulates contact sites between vacuoles and mitochondria. *Dev. Cell* 30: 86–94.
41. González Montoro, A., K. Auffarth, C. Hönscher, M. Bohnert, T. Becker, B. Warscheid, F. Reggiori, M. van der Laan, F. Fröhlich, and C. Ungermann. 2018. Vps39 interacts with Tom40 to establish one of two functionally distinct vacuole-mitochondria contact sites. *Dev. Cell.* 45: 621–636.e7.
42. Kagan, J. C., M. P. Stein, M. Pypaert, and C. R. Roy. 2004. *Legionella* subvert the functions of Rab1 and Sec22b to create a replicative organelle. *J. Exp. Med.* 199: 1201–1211.
43. Flanagan, J. J., I. Mukherjee, and C. Barlowe. 2015. Examination of Sec22 homodimer formation and role in SNARE-dependent membrane fusion. *J. Biol. Chem.* 290: 10657–10666.
44. Gillingham, A. K., R. Sinka, I. L. Torres, K. S. Lilley, and S. Munro. 2014. Toward a comprehensive map of the effectors of rab GTPases. *Dev. Cell* 31: 358–373.
45. Spang, A. 2016. Membrane tethering complexes in the endosomal system. *Front. Cell Dev. Biol.* 4: 35.
46. Stefan, C. J., A. G. Manford, and S. D. Emr. 2013. ER-PM connections: sites of information transfer and inter-organelle communication. *Curr. Opin. Cell Biol.* 25: 434–442.
47. Rieusset, J. 2018. The role of endoplasmic reticulum-mitochondria contact sites in the control of glucose homeostasis: an update. *Cell Death Dis.* 9: 388.
48. Schwarz, K., Y. Schröder, B. Qu, M. Hoth, and H. Rieger. 2016. Optimality of spatially inhomogeneous search strategies. *Phys. Rev. Lett.* 117: 068101.
49. Monzon, G. A., L. Scharrel, L. Santen, and S. Diez. 2018. Activation of mammalian cytoplasmic dynein in multimotor motility assays. *J. Cell Sci.* 132: jcs220079.
50. Mitra, A., F. Ruhnow, S. Girardo, and S. Diez. 2018. Directionally biased sidestepping of Kip3/kinesin-8 is regulated by ATP waiting time and motor-microtubule interaction strength. *Proc. Natl. Acad. Sci. USA* 115: E7950–E7959.
51. Zhou, X., R. Zhao, K. Schwarz, M. Mangeat, E. C. Schwarz, M. Hamed, I. Bogeski, V. Helms, H. Rieger, and B. Qu. 2017. Bystander cells enhance NK cytotoxic efficiency by reducing search time. *Sci. Rep.* 7: 44357.
52. Raiborg, C., E. M. Wenzel, and H. Stenmark. 2015. ER-endosome contact sites: molecular compositions and functions. *EMBO J.* 34: 1848–1858.
53. Eden, E. R. 2016. The formation and function of ER-endosome membrane contact sites. *Biochim. Biophys. Acta* 1861(8 Pt B): 874–879.
54. Raiborg, C., E. M. Wenzel, N. M. Pedersen, H. Olsvik, K. O. Schink, S. W. Schultz, M. Vietri, V. Nisi, C. Bucci, A. Brech, et al. 2015. Repeated ER-endosome contacts promote endosome translocation and neurite outgrowth. *Nature* 520: 234–238.
55. Marwaha, R., S. B. Arya, D. Jagga, H. Kaur, A. Tuli, and M. Sharma. 2017. The Rab7 effector PLEKHM1 binds Arl8b to promote cargo traffic to lysosomes. *J. Cell Biol.* 216: 1051–1070.